



Substructure Evolution and Mechanical Properties in Martensitic Stainless Steel During a High Cycle Number of Repetitive High Stress Loading–Unloading Process

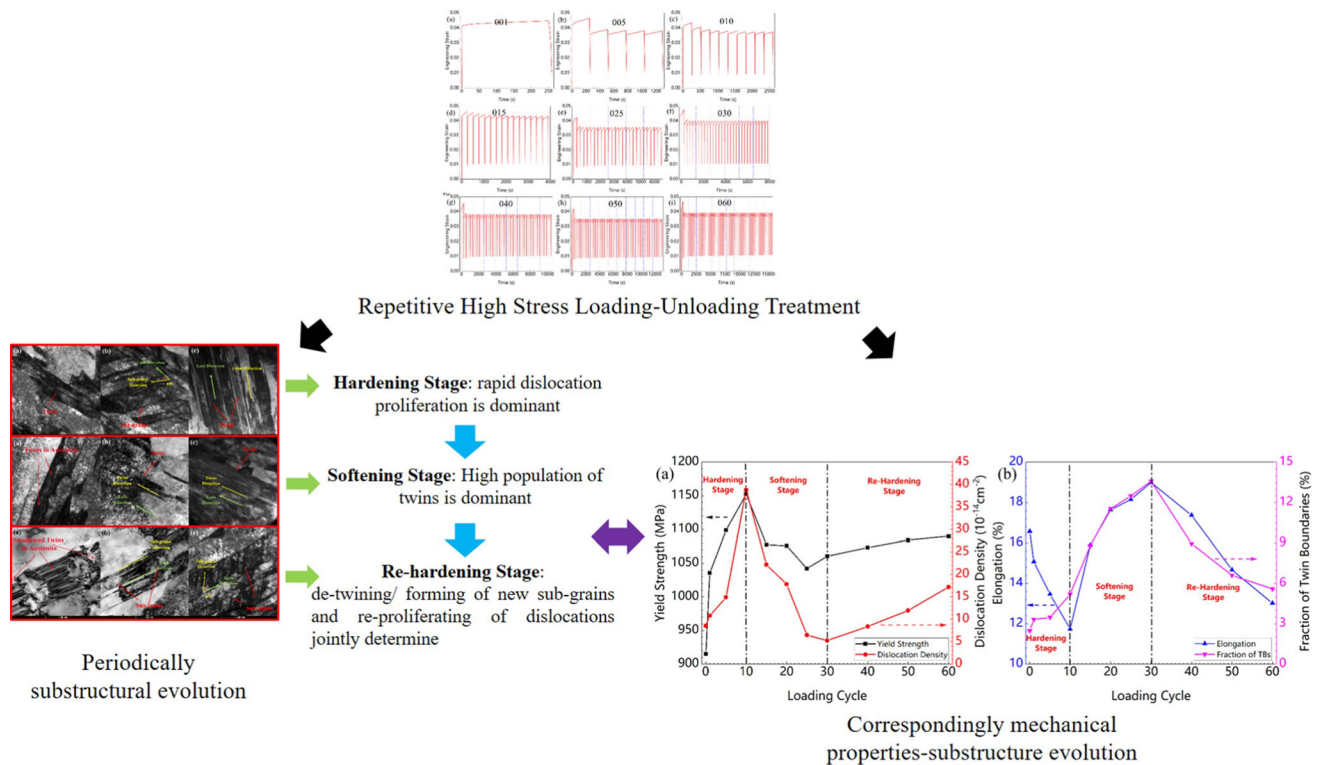
YUDAO WEI, HENGCHENG LIAO, ZHENLIN LAN, and HONG LING

The influence of the loading cycle number in repetitive high stress loading/unloading (RHSL) treatment on the substructure evolution in a martensite stainless steel and mechanical properties was studied by mechanical property test and microstructure characterization. From the results of strain-time curves of all samples, it is seen that total 60 cycles RHSL treatment only produces tiny plastic deformation (residual strain less than 0.011) with a low strain rate (less than $128 \times 10^{-3} \text{ s}^{-1}$). It is concluded that the evolution of deformation twins in the A-steel during total 60 cycles of RHSL treatment experiences 3 stages, early nurturing (Stage I, the first 10 cycles), medium-term abundantly forming (Stage II, the middle 20 cycles) and later de-twinning (Stage III, the last 30 cycles). The variation of mechanical properties of the A-steel during total 60 cycles of RHSL treatment can also be divided into corresponding 3 stages, dislocations-induced strain-hardening stage (Stage I), twins-predominant structure-softening stage (Stage II) and dislocations/twins co-determined re-hardening stage (Stage III). Even YS is non-monotonically varying with the dislocation density, it is found that the variation of yield strength is strongly correlated with the increase or decrease of dislocations induced by the RHSL treatment, and the elongation is highly related to the fraction of twins existing. The A-steel treated by 30-cycle RHSL at room temperature with the holding stress close to the yield strength and the loading time of 0.64 seconds has the highest fraction of twins (13.58 pct TBs), possesses a high yield strength (1060 MPa), the highest elongation (19.0 pct) and the highest PSES value (2195 MPa·pct).

YUDAO WEI is with the Jiangsu Key Laboratory for Advanced Metallic Materials, School of Materials Science and Engineering, Southeast University, Nanjing 211189, P.R. China and also with the Sensors & System Research Department, The 48th Research Institute of China Electronics Technology Group Corporation, Changsha 410111, P.R. China. HENGCHENG LIAO is with the Jiangsu Key Laboratory for Advanced Metallic Materials, School of Materials Science and Engineering, Southeast University. Contact e-mail: hengchengliao@seu.edu.cn ZHENLIN LAN and HONG LING are with the Sensors & System Research Department, The 48th Research Institute of China Electronics Technology Group Corporation.

Manuscript submitted March 4, 2024; accepted July 24, 2024.

Article published online August 9, 2024



<https://doi.org/10.1007/s11661-024-07537-y>

© The Minerals, Metals & Materials Society and ASM International 2024

I. INTRODUCTION

MARTENSITIC stainless steels are widely used in many important constructive applications due to its excellent combination of strength and toughness. The microstructure of them presents highly inhomogeneity, involving in martensite lath groups with high-density of dislocations inside the fine laths and dispersed residual austenite in blocky or film forms inserted between laths or lath groups.^[1–6]

The substructure of martensitic lath has a decisive influence on its strength and toughness. In general, the substructure of low carbon martensite is dominated by dislocations and supplemented by twins.^[6] The formation of twins in martensite roots in phase transformation or deformation, and the morphology of them is similar to closely packed bamboo leaves or a fully loaded submachine gun magazine.^[7,8] During the deformation process, the strain energy in martensite laths could be released through the deformation by crystallographic plane symmetry, which is a way of crystal self-adjustment,^[9–11] thus, twins is prone to form.

Many researchers point out that microstructure optimization, such as introducing deformation twins,^[12–15] is an effective method to further improve their mechanical properties. In this way, the strength and plasticity are expected to be enhanced simultaneously because of the obstructing effect of twin boundaries to dislocation slip and the interaction between twins and dislocations.^[16–20]

Such strategy has been adopted in carbon steels, martensite Ti alloys and Ni alloys. In the martensite Ti–6Al–4V alloy, an excellent ductility with a cold-rolling ability of more than 40 pct reduction was thought to be due to the fine equiaxed grains with {1011} twins.^[21] A new β Ti–1Mo–2V alloy exhibited high yield strength (693 MPa), high ultimate tensile strength (857 MPa) and large total elongation (31.8 pct) and such excellent strength–ductility synergy originated from successively activated primary (332)[113] twins and secondary (112)[111] twins.^[22] Fe–Mn–C steel was strengthened significantly (with yield strength increased from 357 to 1275 MPa) by the introduction of ϵ -martensite nanotwins.^[23] In Ni–Mn–Ga alloy, [011] and [111] twins were introduced and the compressive stress and strain were 2630 MPa and 54 pct, respectively.^[24] The generation of deformation twins depends on the strain rate,^[25,26] temperature,^[27,28] loading time,^[29] loading stress,^[30] and loading cycles.^[31]

In our previous study, the substructure evolution and mechanical properties of S04 martensitic stainless steel with the loading cycle number up to 20 in the RHSL (repetitive high stress loading–unloading) treatment has been deeply discussed in Reference 32. The generation mechanism of deformation twins in another martensitic stainless steel (abbreviated as MS-steel in Reference 33; uniformly as A-steel in subsequent articles) during a 20-cycle RHSL treatment with different loading rates of

force (corresponding to different strain rates) has been reported in Reference 33. The mechanical properties of S04 steel underwent a hardening-softening transformation during the 20-cycle RHSL treatment, corresponding to different microstructure evolution.^[32] In the hardening stage (the first 10 cycles), the dislocations were significantly proliferated and greatly piled-up; in the softening stage (the second 10 cycles), twinning was widely triggered by the severe stress concentration. Finally, the 20-cycle RHSL treatment led to a synthetically optimization of mechanical properties, where the yield strength was increased by about 20 pct as well as a rise in the impact toughness by 10 pct. Different from the traditional method for twin generation by one-off deformation under super loading stress with huge plastic deformation or under super-high strain rate,^[34–38] the novel 20-cycle RHSL treatment at room temperature successfully generated abundant deformation twins in the MS-steel.^[33] In the RHSL treatment, the strain rate was much small, less than $1.5 \times 10^{-1} \text{ s}^{-1}$ and the produced residual strain was very small (not more than 0.01). The fraction and the morphology diversity of twins were increased with the loading rate of force.

However, the above RHSL treatment ended up at the 20th cycle. The evolution of substructure and variation of mechanical properties with further cyclic loading–unloading have not been well established. Obviously, it is of importance to verify the further evolution of deformation twins and the corresponding change of mechanical properties. Thus, in this study, the A-steel was RHSL-treated with high loading–unloading cycle number at room temperature. XRD, EBSD and TEM were applied to characterize the microstructure evolution while tensile test was utilized to examine the mechanical properties.

II. EXPERIMENTAL

A. Sample Preparation and RHSL Treatment

In this study, the selected martensitic stainless steel (abbr. as the A-steel) was fabricated by hot extrusion from Central Iron and Steel Research Institute (Beijing, China). It has a mean yield strength ($\sigma_{0.2}$) of about 927 MPa.^[33] The composition of the A-steel is: 0.057 C, 15.86 Cr, 0.39 Mn, 6.35 Ni, 0.014 P, 0.007 S, 0.46 Si and balanced Fe (in wt pct), same as MS-steel in Reference 33. The sample preparation and RHSL treatment were reported in Reference 33. The original state of A-steel is denoted as OS in this study. As shown in Figure 1, rod-like samples with a circular gauge part of ϕ 10 mm \times 84 mm were cut from the same batch of OS A-steel ingot for the RHSL treatment in this study.

A whole cycle of the RHSL treatment contains a loading stage (to the target loading force of 72806 N within 0.64 seconds in this study), a holding stage (holding time of 250 seconds) with the applied engineering stress, 927 MPa, equal to the mean yield strength of the A-steel in original state (OS), and an unloading stage (to several dozens of Newtons within 10 seconds).^[32,33] The cycle number of the RHSL treatment

of was adjusted in this study. Sample No. are named by the corresponding holding stress and loading cycle number. Details of the RHSL treatment in this study are listed in Table I. Residual strain is defined as a ratio between the measured gauge length of the loaded sample at the end of every RHSL cycle and the original gauge length.

B. Microstructure Characterization and Tensile Test

Sirion field emission scanning electron microscopy (FEI) was employed for the EBSD (electron backscattered diffraction) characterization of substructure in the samples in different states. Thin sheets for EBSD samples were cut from the OS cylinders and the middle part of RHSL-treated samples, and then prepared by twin-jet electro polishing obtain more reliable results. Due to the hyperfine microstructure of the A-steel, 5 random regions of 30 $\mu\text{m} \times$ 25 μm were scanned on each sample. The statistical data obtained from the five scanning regions were averaged for each sample. Channel 5 software was used to analyze the obtained EBSD data. The details of the operation for the EBSD data treatment were introduced in our previous study.^[33]

Evolution of substructures like twins and sub-grains was characterized by a FEI-made G²⁰ transmission electron microscopy (TEM). Sheets for TEM sample were also first cut from an OS cylinder and the middle part of RHSL-treated samples, and then reduced by twin-jet electro polishing. SAED (selected area electronic diffraction) patterns were calibrated. X-ray diffraction analyzer (D8-Discover) using Cu K α radiation ($\lambda = 1.54 \text{ \AA}$) was adopted to characterize the phase constituents and to estimate the dislocation density in it.

According to GB/T228.1-2010,^[39] tensile test was operated at a rate of 1 mm min⁻¹ on small tensile samples with a square gauge part of 1.6 mm \times 1.6 mm \times 26 mm (shown in Figure 2) which were also cut from the OS and RHSL-treated samples with different cycles. In our tensile test, an extender with a gauge of 10 mm was used. The data of Young's modulus and yield strength were given directly by the tensile system software with the extender. The data of mechanical properties were the mean of three tested samples.

C. Estimation of Dislocation Density

On the basis of the structural information obtained from XRD diagrams, modified WH (Williamson–Hall) method can be applied to estimate the dislocation density in the tested samples, as following^[40]:

$$\Delta K^D = A \left(\frac{\pi \rho b^2}{2} \right)^{\frac{1}{2}} K C^{\frac{1}{2}} + A' \left(\frac{\pi \rho b^2}{2} \right)^{\frac{1}{2}} K^2 C, \quad [1]$$

where ΔK^D is the strain contribution to the line broadening, A and A' the parameters determined by the effective outer cut-off radius of dislocations and other auxiliary parameters without any physical interpretation, ρ the average dislocation density, b the dislocation Burgers vector, C the average contrast factor of dislocations for a particular reflection to take into

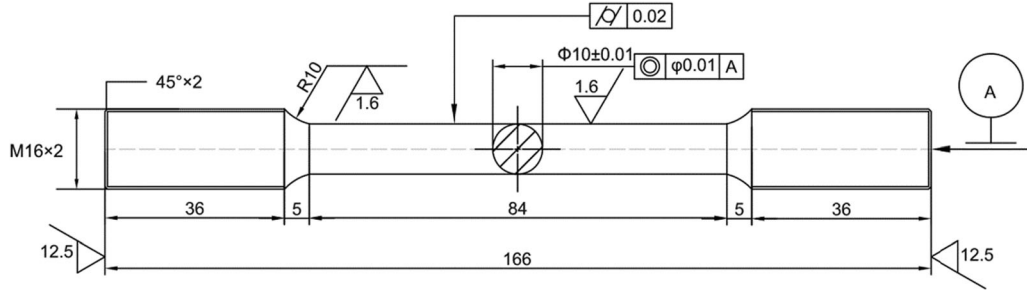


Fig. 1—Shape and size (in mm) of the rod-like sample for RHSL treatment.

account the contrast effect of dislocations on peak broadening. The expressions of ΔK^D and K are given as following:

$$\Delta K^D = \Delta K - \frac{0.9}{D}, \quad [2]$$

$$K = \frac{2\sin\theta}{\lambda}, \quad [3]$$

$$\Delta K = \frac{2\cos\theta(\Delta\theta)}{\lambda}, \quad [4]$$

$$D = \frac{\lambda}{2\sin\theta}, \quad [5]$$

where D is the mean grain size, λ the wave length of X-ray, θ the diffraction angle.

Combining with Eqs. [2] through [5], Eq. [1] can be deformed as following:

$$\frac{2\cos\theta(\Delta\theta)}{\lambda} = \frac{2\sin\theta}{\lambda} \left[0.9 + A \left(\frac{\pi\rho C b^2}{2} \right)^{\frac{1}{2}} \right] + 4A' \left(\frac{\pi Q b^2}{2} \right)^{\frac{1}{2}} \left(\frac{\sin\theta}{\lambda} \right)^2 C. \quad [6]$$

According to Reference 41, Q can be expressed as following:

$$Q = \frac{4Q^*}{\lambda(\pi g^2 b^2 C)^2}, \quad [7]$$

where Q^* is the formal sense of Q , g the particular reflection. As for Q^* , it can be expressed as following^[41]:

$$Q^* = \langle \rho^{*2} \rangle - \langle \rho^* \rangle^2, \quad [8]$$

where ρ^* is the formal dislocation density, and the operational character “ $\langle \rangle$ ” is to get the mean value of a series data. Here, the series of dislocation density has only one data for each sample. Hence, $\langle \rho^{*2} \rangle = \langle \rho^* \rangle^2$ and it can get the values of both Q^* and Q to be 0. Further, the value of $4A' \left(\frac{\pi Q b^2}{2} \right)^{\frac{1}{2}} \left(\frac{\sin\theta}{\lambda} \right)^2 C$ is 0. Thus, Eq. [6] can be changed as following:

$$\frac{2\cos\theta(\Delta\theta)}{\lambda} = \frac{2\sin\theta}{\lambda} \left[0.9 + A \left(\frac{\pi\rho C b^2}{2} \right)^{\frac{1}{2}} \right]. \quad [9]$$

Since θ is a constant value for each sample, the value of infinitely small quantity $\Delta\theta$ can be approximately taken as 0. Finally, the dislocation density ρ can be expressed as following:

$$0 = \frac{2\sin\theta}{\lambda} \left[0.9 + A \left(\frac{\pi\rho C b^2}{2} \right)^{\frac{1}{2}} \right], \quad [10]$$

$$\rho = \frac{2 \times 0.9^2}{\pi A^2 b^2 C}. \quad [11]$$

From Wilkens theory, for a wide range of dislocation distribution, the value of A can be taken as $A = 0.316$ (i.e., $\frac{1}{A^2} = 10$).^[42] Reference 43 mentions the average ‘ C ’ factors of pure edge and pure screw dislocations for different diffraction vectors calculated numerically using ANIZC computer code for the [110] {111} slip systems and by applying the single crystal elastic constants of BCC iron, where C_{pureedge} and $C_{\text{purescrew}}$ are 0.1795 and 0.1057, respectively. It is assumed that edge and screw dislocations are split in half in the steel. Hence, the C value is taken as 0.1426 here.

D. Strain-Hardening Exponent Determination

To assess the service safety in engineering, the strain-hardening exponent (n), can be obtained from the true stress–true strain curve.^[44] This exponent represents the degree of deformation hardening capacity or the ability to resist sustaining plastic deformation of a metallic material, Universally, Hollomon equation is used to describe the strain-hardening effect of metallic materials during plastic deformation, seeing Eq. [12]^[44]:

$$\sigma_T = K \varepsilon_T^n. \quad [12]$$

For convenient calculation, logarithm is taken on Eq. [12] to get Eq. [13] as following:

$$\ln\sigma_T = n \ln\varepsilon_T + \ln K, \quad [13]$$

Table I. Details of the RHSL Treatment in this Study

Sample No.	Target Force (N)	Nominal Holding Stress (MPa)	Loading Time (s)	Loading Rate of Force (N·s ⁻¹)	Loading–Unloading Cycle
927-001	72,806	927	0.64	113,760	1
927-005					5
927-010					10
927-015					15
927-020*					20
927-025					25
927-030					30
927-040					40
927-050					50
927-060					60

*RHSL treatment of the 927-020 sample has been processed in Ref. [33] named as A-5 sample. For this sample, all related RHSL treatment data and EBSD data are quoted from Ref.[33].

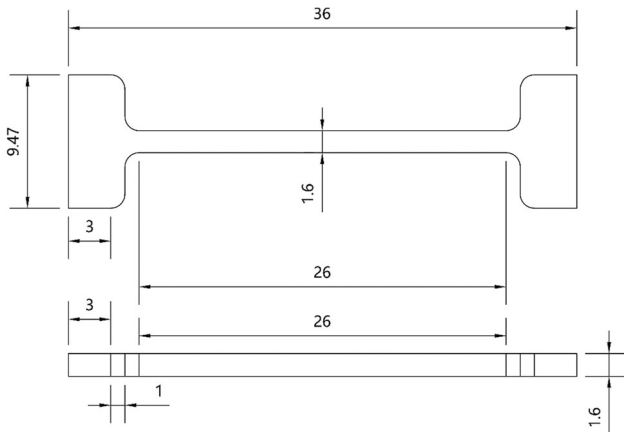


Fig. 2—Shape and size (mm) of sample for tensile test.

where the true stress (σ_T) and true strain (ϵ_T) data are gotten from the uniform deformation stage of the tensile curves. They are calculated from the engineering stress (σ) and engineering strain (ϵ) data by the following equations (GB/T 5028-2008)^[45]:

$$\sigma_T = \sigma(1 + \epsilon), \quad [14]$$

$$\epsilon_T = \ln(1 + \epsilon). \quad [15]$$

By fitting the logarithm data of $\ln\sigma_T$ – $\ln\epsilon_T$, the slope of fitting line is finally obtained, namely the n value.

III. RESULTS

A. Strain and Strain Rate

Figure 3 illustrates the engineering strain-time curves of samples during the RHSL treatment. Figure 4 illustrates engineering strain-time curves in the 1st, the 10th and the last cycle for the representative 927-060-sample. In the 1st cycle, obvious plastic deformation can be seen at the holding stage; when the treatment comes to the 10th cycle, plastic deformation at the holding stage becomes much less but visible; as

the loading–unloading cycle was carried on, deformation at the holding stage is still considerable even in the 60th cycle.

Figures 5(a) and (b) show the variation of residual strain of all RHSL-treated samples with the cycle number and the increment of residual strain during each cycle for 927-030-sample and 927-060-sample, respectively. Residual strain produced in the 1st cycle takes up the most major fraction. When the loading cycle exceeds 5, the increment of residual strain can be nearly negligible. Notably, the total residual strain values of each sample are different, fluctuating in a very limited range.

For each sample, the maximal strain always occurs in the first cycle (seen in Figure 3), and, correspondingly, the maximal strain rate is also obtained in this cycle. For all these samples, the highest strain rate is $1.28 \times 10^{-1} \text{ s}^{-1}$, calculated by the same method in Reference 33. Moreover, the maximal total residual strain among all samples is less than 0.011. This suggests that the RHSL treatment even with 60 cycles only produces tiny plastic deformation and the strain rate is very low.

B. Distribution and Statistical Information of Sub-grains and Twins

Figure 6 illustrates the representative morphology and distribution of martensite phase (red) and residual austenite phase (yellow) in the samples in OS and RHSL-treated states, where, martensite laths are the major phase while the blocky or film-like austenite is the minor one in this steel. The microstructure is significantly inhomogeneous, containing much high fraction of a variety of boundaries and different lath directions. After the RHSL treatment at the holding stress of 927 MPa, even with 60 cycles, the boundaries of martensite laths are still distinct, suggesting that the plastic deformation occurred during the RHSL treatment is rather slight.

Figure 7 illustrates the representative grain boundary distribution maps in the samples, where the yellow lines, blue lines and red lines represent for the low-angle grain boundaries (LAGBs, misorientation angle between

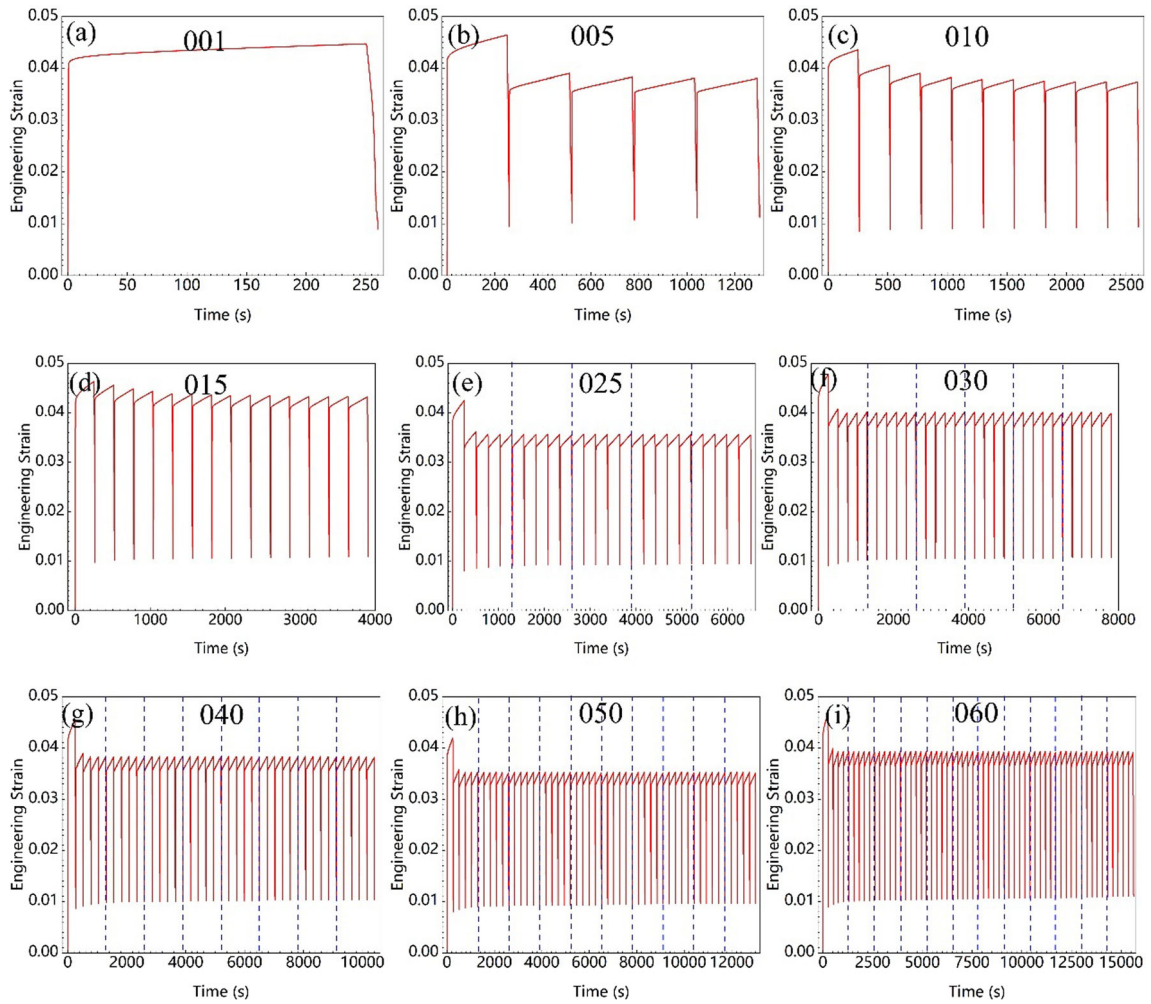


Fig. 3—Engineering strain–time curves of each sample during the RHL treatment: (a) 927-001-sample, (b) 927-005-sample, (c) 927-010-sample, (d) 927-015-sample, (e) 927-025-sample, (f) 927-030-sample, (g) 927-040-sample, (h) 927-050-sample, and (i) 927-060-sample.

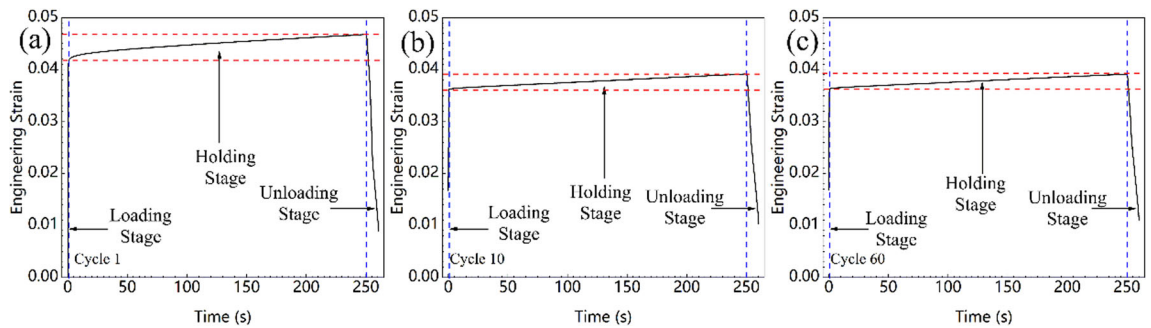


Fig. 4—Engineering strain–time curves in the first cycle (a), the 10th cycle (b) and the last cycle (c) for the 927-060-sample.

adjacent grains of 2 to 15 deg) and high-angle grain boundaries (HAGBs, misorientation angle larger than 15 deg) and twin boundaries (TBs, defined as the $\Sigma 3$ boundaries^[46] where one part of the grain rotates 60 deg rolling around [111] orientation, symmetrical with another part), respectively. It can be seen that the density of TBs is increased from OS sample to 927-030-sample, and decreased from 927-030-sample to 927-060 sample. Especially, high-density TBs exist in

927-020-sample, 927-025 sample, 927-030 sample and 927-040 sample.

Figure 8 illustrates the misorientation angle distribution (MAD, from 0 to 65 deg) of all samples. The fractions of SGBs (sub-grain boundaries, misorientation angle between adjacent grains less than 2 deg,^[47,48] on the left of the dotted line in each figure), LAGBs, HAGBs and TBs are denoted in these plots. In most

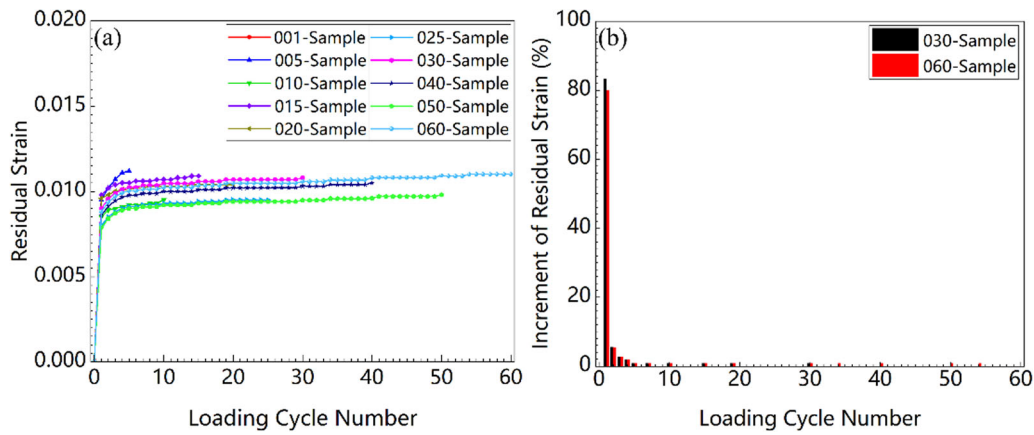


Fig. 5—Residual strain of all RHSL-treated samples with the cycle number (a) and the increment of residual strain during each cycle (b) of 927-030- and 927-060-samples as the examples (b).

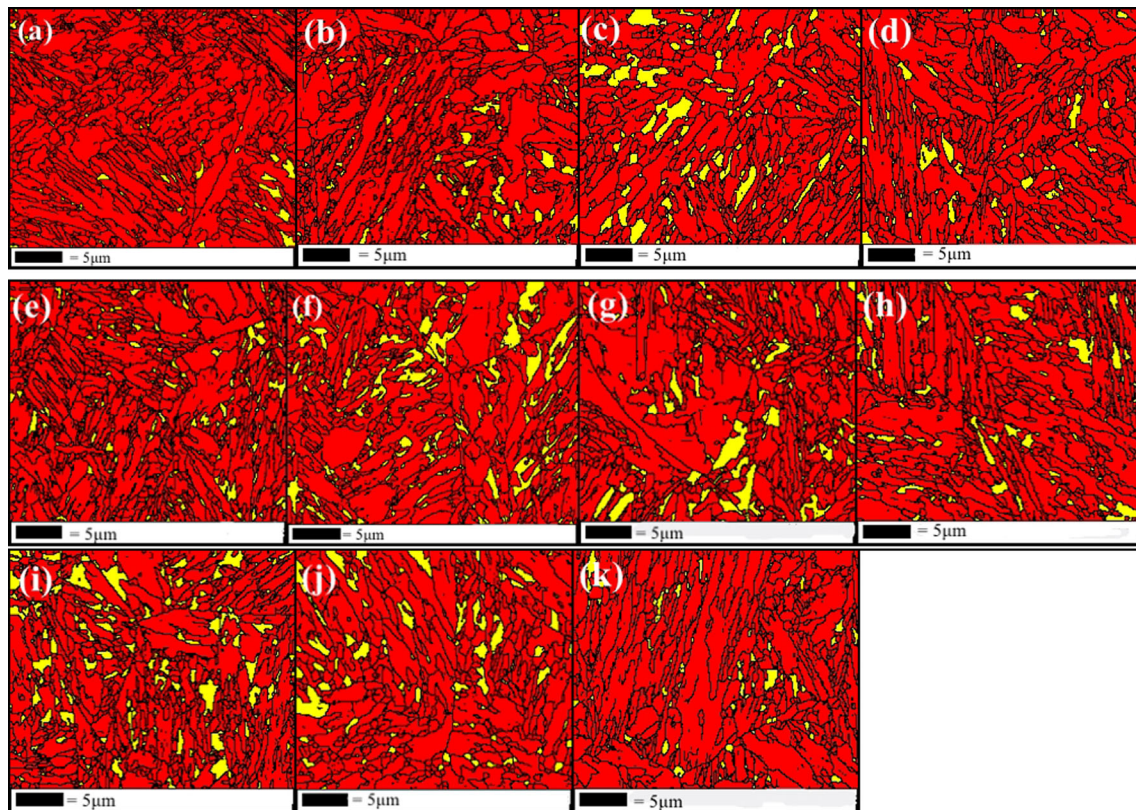


Fig. 6—Phases distribution (red: martensite; yellow: austenite) and grain morphology in the samples with/without the RHSL treatment: (a) OS sample, (b) 927-001-sample, (c) 927-005-sample, (d) 927-010-sample, (e) 927-015-sample, (f) 927-020-sample, (g) 927-025-sample, (h) 927-030-sample, (i) 927-040-sample, (j) 927-050-sample, and (k) 927-060-sample (Color figure online).

statistical analysis on MAD, sub-grain boundaries are usually neglected.

However, in this study, the substructure evolution involves in de-twinning into sub-grains during the RHSL treatment, thus, the variations of the fractions of twins and sub-grains are focused on. In the OS state, the A-steel has experienced hot extrusion. Of importance, in one martensite lath group, sub-grain orientation relationship exists between laths.^[47] Therefore, on the whole, the primary part of the boundaries in all

samples locates in the range of misorientation angle between adjacent grains less than 2 deg. Sub-grain is the main component of substructure in this steel, and the statistical data in Figure 8 indicate the HAGBs in the studied samples mainly range from 50 to 62 deg. It should be noted that because the fraction of austenite phase is small and especially the size of austenite grains is too small, the TBs in austenite weren't marked (be ignored) and not included in the statistical data in Figures 7 and 8 by Channel 5 software.

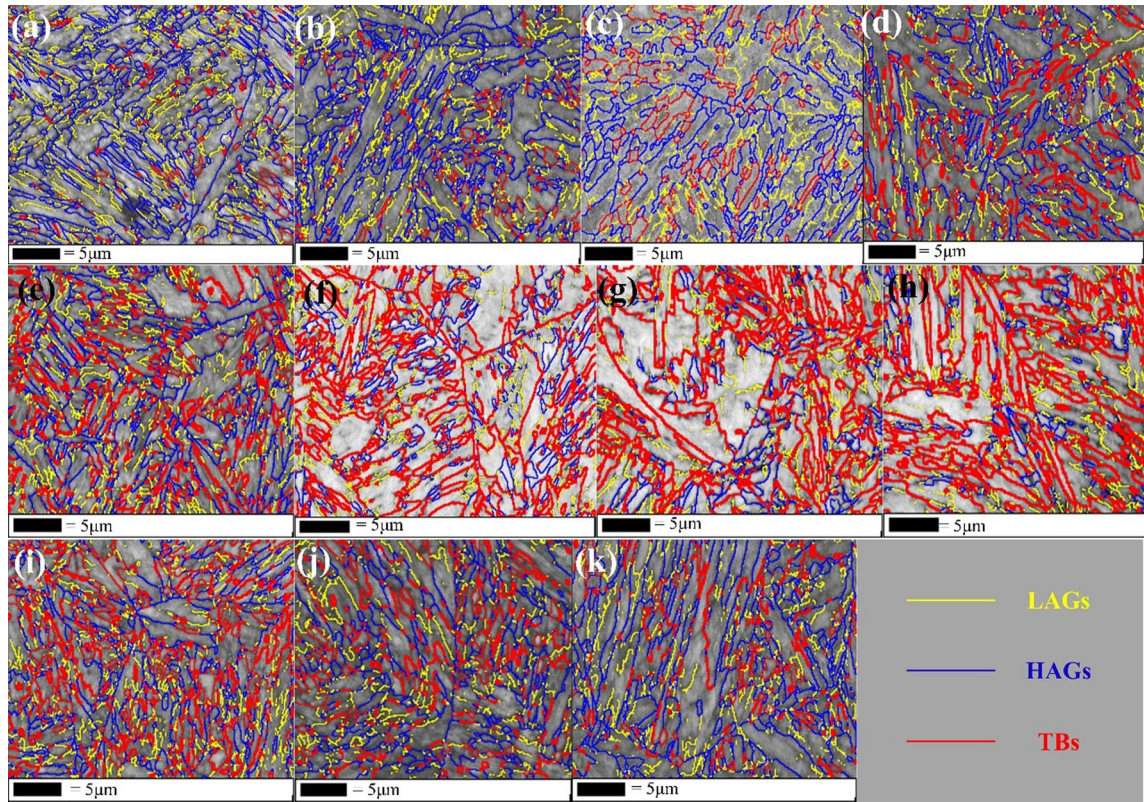


Fig. 7—Grain boundary distribution in the samples with/without the RHSL treatment: (a) OS sample, (b) 927-001-sample, (c) 927-005-sample, (d) 927-010-sample, (e) 927-015-sample, (f) 927-020-sample, (g) 927-025-sample, (h) 927-030-sample, (i) 927-040-sample, (j) 927-050-sample, (k) 927-060-sample.

The fractions of TBs and SGBs with the cycle number are illustrated in Figure 9(a). The area/number fractions of twinning grains (defined as in Reference 33) are exhibited in Figure 9(b). For the fraction of TBs, it is first increased from 2.48 pct (0 cycle) to 13.58 pct (30 cycles), and then decreased to 6.61 pct (60 cycles); for the fraction of SGBs, it is first decreased from 76.09 pct (0 cycle) to 65.36 pct (30 cycles), and then increased to 80.08 pct (60 cycles); for the area fraction of twinning grains, it is first increased from 1.53 pct (0 cycle) to 9.89 pct (30 cycles), and then decreased to 3.07 pct (60 cycles); for the number fraction of twinning grains, it is first increased from 5.23 pct (0 cycle) to 13.68 pct (25 cycles), and then decreased to 9.05 pct (60 cycles). In general, the variations of the fractions of twins and sub-grains with the loading cycle number can be divided into three stages: In Stage I (the first 10 cycles), the fraction of twins slightly rises and that of the SGBs declines; in Stage II (the middle 20 cycles), the fraction of twins remarkably rises and that of the SGBs keeps declining. The sample treated by around 30 cycles contains the highest fraction of twins and the lowest fraction of sub-grains; in Stage III (the last 30 cycles), the fraction of SGBs experiences a significant rise accompanying with a great decrease in the fraction of twins, suggesting the probability of a transformation relation between the twins and sub-grains.

C. Microstructural Evolution After the RHSL Treatment

Details of the SAED patterns of deformation twins in martensite and austenite in the studied samples are summarized in Table II from SAED patterns in Reference 33. Follow the below steps, the orientation of grains containing twins can be determined: First, draw one smallest parallelogram in the SEAD pattern and calculate the two orientations according to the included angle and the martensite crystal orientation list (easy to get online); Second, try to choose one side (orientation) of the parallelogram to be the public orientation, sign its opposite vector quantity as one side (orientation) of another parallelogram, and calculate another side (orientation) according to the included angle and the martensite crystal orientation list (easy to get online); Finally, if the two parallelograms have the same calculated grain axis (twinning axis), the orientation of grains containing twins can be determined. Additionally, the twinning axis must be vertical to the twinning plane.

In crystallography, larger orientation index relates to smaller interplanar spacing.^[49] Three types of twins, Types A to C, are observed in martensite of MS-steel (A-steel) in Reference 33, in which one of the orientation indexes steadily belongs to [101] series and the other changes from [220] to [123]. Additionally, both Types A and C twins belong to the $\{112\}(111)$ twinning system, which are the common deformation twins in BCC alloys; Type B twins belong to the $\{332\}(113)$ twinning

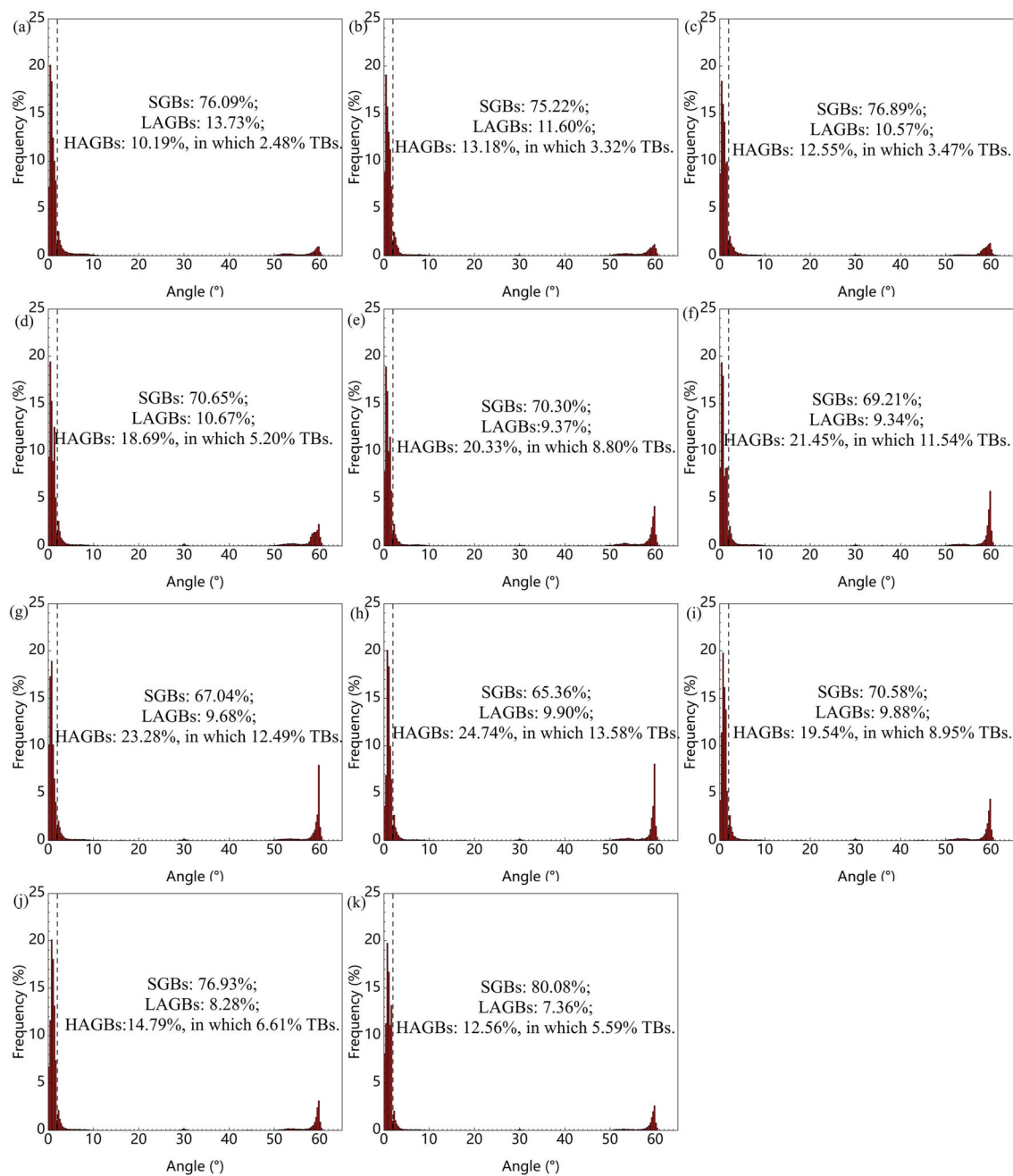


Fig. 8—Misorientation angle distribution (MAD) of samples in different states: (a) OS sample, (b) 927-001-sample, (c) 927-005-sample, (d) 927-010-sample, (e) 927-015-sample, (f) 927-020-sample, (g) 927-025-sample, (h) 927-030-sample, (i) 927-040-sample, (j) 927-050-sample, and (k) 927-060-sample.

system, which were reported in the impact-loaded α -Fe and β -Ti alloys.^[50,51]

The microstructure of OS sample and 927-020-sample has been discussed in Reference 33. For OS sample, the microstructure was mainly constituted of martensite lath groups with high-density of dislocations inside as the substructure; in addition, residual austenite was clamped between the laths as the secondary phase. As supplementary information, lath groups of martensite and sub-grains in the OS sample are shown in Figure 10. As shown in Figure 10(a), lath groups of martensite with

different orientations are the basic element of substructure in the OS sample. One lath group consists of many small and approximately parallel laths (Figure 10(b)). Most of laths are with a width of 100 to 200 nm and some with more width. SAED patterns in Figures 10(c) through (e) (corresponding to the laths marked by (c), (d) and (e) in Figure 10(b), respectively) demonstrate the sub-grain orientation relationship between these laths. When austenite transforms into martensite, one austenite grain becomes many martensite grains (lath groups). Each martensite grain composes of many small and

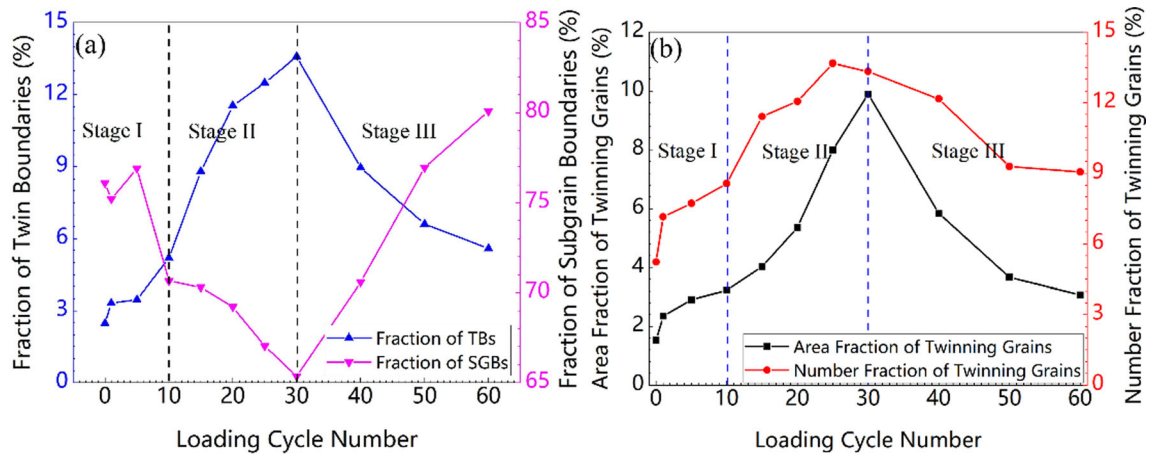


Fig. 9—Fractions of TBs and SGBs (a) and area fraction and number fraction of twinning grains (b) with the loading cycle number.

approximately parallel laths that are with the orientation relationship of sub-grains (with orientation difference less than 2 deg).^[52,53] In some coarse laths, many fine laths with a width of tens of nanometers are observed (Figures 10(f) and (g)), which are with a certain angle to the coarse-lath direction. When the diffraction grating covers these fine laths, there is only one sort of diffraction spots (Figure 10(h)) that demonstrates they are in the orientation relationship of sub-grains. The A-steel in the OS state has experienced hot extrusion, thus the existence of fine sub-grains in coarse martensite laths is probable. Because of the sub-grain orientation relationship between laths in a martensite lath group and the existence of fine sub-grains inside the coarse laths, EBSD illustrates a very high fraction of SGBs (76.1 pct, seen in Figure 8(a)). In the later elaboration on the substructure evolution, the above microstructure features of sub-grains as in OS state will not be focused on. The focus is on the generation of twins and the new sub-grains formed by detwinning.

Figures 11 and 12 show the TEM observation on 927-001 sample and 927-005 sample, respectively. When the sample experienced only 1 cycle of RHSL treatment, its microstructure did not change obviously compared to the OS sample. Lens-like austenite is still nearly clean with very few lines of stacking faults (SFs, Figures 11(a) and (c)), and martensite lath groups keep the original morphology (Figures 11(b) and (d)). As the loading cycle number slightly increases to 5, more lines of SFs in austenite are observed (Figure 12(a)) which are demonstrated by the distinct streakings in the SAED pattern (Figure 12(c)). No considerable change occurs in martensite laths (Figures 12(b) and (d)).

However, when the loading cycle number reaches to 10, some important evolutions in microstructure are occurring. Twins transmitted from dense SFs are observed in austenite (Figures 13(a) and (d)). Sub-grains with a width from tens of nanometers to about one hundred nanometers are formed in martensite laths (Figures 13(b) and (e)), at an angle of about 55 deg to the lath direction. This type of sub-grains is rarely observed in the OS sample. Simultaneously, Type C twins in bunches with a length of a few micrometers and a

width of tens of nanometers are observed in a very coarse martensite lath (Figures 13(c) and (f)), almost parallel to the lath direction. This suggests that deformation twins start forming at this stage. As reported in Reference 32, twins also began to generate in S04 martensite stainless steel with 10-cycle RHSL treatment at 93 K. The generation of twins is derived by the accumulated strain energy and high-density of dislocations.^[32,33]

As the loading cycle number increases to 15, single-orientation twins can be seen in austenite (Figures 14(a) and (d)). In martensite, Type C twins with a width of tens of nanometers parallel to the lath direction (Figures 14(b) and (e)) and similar ones of Type B (Figures 14(c) and (f)) are frequently observed inside laths. For 927-020-sample, 3 types of twins (Types A, B and Type C) in martensite and intersecting twins in austenite were the important and fundamental components in the substructure.^[33] As the loading cycle number arrives to 25, single-orientation SFs can be seen in austenite (Figures 15(a) and (c)). In martensite, Type A twins with a width of tens of nanometers and parallel to the lath direction (Figures 15(b) and (d)) and similar ones of Type B (Figures 15(e) and (g)) at a certain angle to the lath direction are observed. In the left-bottom of Figure 15(f), very tiny twins of Type B (demonstrated by the SAED pattern in Figure 15(h)) are observed in martensite lath, interestingly with a certain angle (40 deg) to the lath direction. In the adjacent upper-right lath, a bunches of sub-grains are forming which is also with a certain angle to the lath direction.

When the loading cycle number comes to 30, single-orientation twins can be seen in austenite (Figures 16(a) and (c)). In martensite, short and thin (Figures 16(b) and (d)) and long and thick (Figures 16(e) and (g)) Type C twins are parallel to the lath direction. Another type of thin twins is seen to be at an angle of about 30 deg to the lath direction (Figures 16(f) and (h)), clarified to be Type B twins.

Summarily, for the formation of twins in martensite, the samples with 10 to 30 cycles of RHSL treatment fall into one category. In this stage of RHSL treatment, the deformation twins start forming obviously in the 927-010 sample, and then multiple orientations/types

Table II. Types of Deformation Twins Distinguished by SAED Patterns in MS-Steel (A-Steel), Summarized from SAED Patterns in Ref. [33]

Phase	Type	Grain Orientation	Index of	
			Twinning Axis	Twinning Plane
Austenite		[111] and [002]	(110)	{111}
Martensite	A	[101] and [220]	(111)	{112}
	B	[101] and [211]	(113)	{332}
	C	[101] and [123]	(111)	{112}

of twins are prosperously and abundantly formed everywhere. The frequency of twins observed in the samples is in agreement with the increase of twin fraction in the curves of Figure 9 obtained from EBSD statistical analysis. Even abundant twins are generated in this stage, but new evolution in substructure is nurturing.

When the loading cycle number continues rising to 40, twins in austenite (Figures 17(a) and (d)) and Type C twins in martensite at an angle of about 50 deg to the lath direction (Figures 17(b) and (e)) are still often observed. But, without doubt, sub-grains are becoming the leader in substructure. As shown in Figures 17(c) and (f), fine sub-grains with a width of tens of nanometers are high-frequently observed in martensite laths, which are at an angle of about 50 deg to the lath direction.

As the loading cycle number goes up to 50, twins in austenite (Figures 18(a) and (d)) are still visible but with sparse twin boundary lines. In martensite laths, twins are difficult to be observed, but fine sub-grains are everywhere, like the ones at an angle of about 55 deg to the lath direction as shown in Figures 18(b) and (d). It is worth to note that, in some laths, the morphology of some substructures (as shown in Figure 18(c)) looks very like twins as shown in Figure 17(b) and the size is very fine (much less than that in Figure 18(b)), but its SAED pattern demonstrates that they are sub-grains (Figure 18(f)). When the loading cycle number finally comes at 60, it is interesting to note that a de-twinning process are happening in austenite (Figure 19(a)), where the twins are seen to be swallowed up by newly formed austenite grains (verified by the same set of diffraction lattice in Figure 19(c)). In martensite laths, sub-grains can be seen everywhere, such as fine and long ones parallel to the lath direction (Figures 19(b) and (d), (e) and (g)), and short and thick ones at an angle of about 60 deg to the lath direction (Figures 19(f) and (h)). Compared to the sub-grains in the OS sample (seen in Figure 10(f)), those in Figures 17(c), 18(b) and 19(g) have a larger width. They might be newly formed during the RHSL treatment.

At this stage from 40th to 60th cycle of RHSL treatment, twins in austenite are gradually disappearing or swallowed up by new austenite grains, and twins in martensite are replaced by sub-grains. TEM observation results on twins and sub-grains are in consistence with

those in Figure 9(a) where the fraction of TBs is decreased while the fraction of SGBs is increased.

Especially, it is worth to note, all sub-grains observed in this study can be classified into three types according the morphology/size and the relationship with the lath direction:

(1) those with a width of larger than 100 nm and parallel to the lath direction (as shown in Figure 10(b), in the OS sample) are the laths in one lath group sharing a sub-grain relationship; they are always observed in the RHSL-treated samples, meaning that they are not changed considerably;

(2) those at an angle to the lath direction and with a width of less than 100 nm, as shown in Figure 13(b) in 927-010 sample, Figure 15(f) in 927-025 sample, Figure 17(c) in 927-040 sample, Figure 18(b) in 927-050 sample and Figure 19(f) in 927-060sample, probably, are newly formed during the RHSL treatment; RHSL treatment induces severe local stress concentration that drives dislocations to slide along specific planes of martensite lath and then to entangle; as a result, dislocation walls are first formed and then sub-graining occurs;

(3) those with a highly similarity in morphology and size of twins (as shown in Figure 18(c) in 927-050 sample and Figures 19(b) and (e) in 927-060 sample) and with approximately same angle relationships to the lath direction (parallel or intersecting). The twin-like sub-grains are of high probability to be transformed from twins. The formation of these fine sub-grains is thought to be related to de-twinning. De-twinning process during RHSL treatment will be dedicated in details in another article.

Summarily, the substructure evolution in the A-steel during a high cycle number of RHSL treatment can be, roughly, divided in to three stages. In Stage I (from the 1st cycle to 10th cycle), repeated loading and holding of applied force results in severe stress concentration due to severe inhomogeneous structure of A-steel. This increasingly drives the nurturing and forming of twins in austenite and martensite in very finite areas. In Stage II (from the 10th to 30th cycle), multiple orientations/types of twins are prosperously and abundantly formed everywhere. In Stage III (from the 30th to 60th cycle), detwinning widely occurs, in other words, twins are gradually disappeared, swallowed up or replaced by newly formed sub-grains. 10 Cycles and 30 cycles of RHSL treatment are two important nodes in the

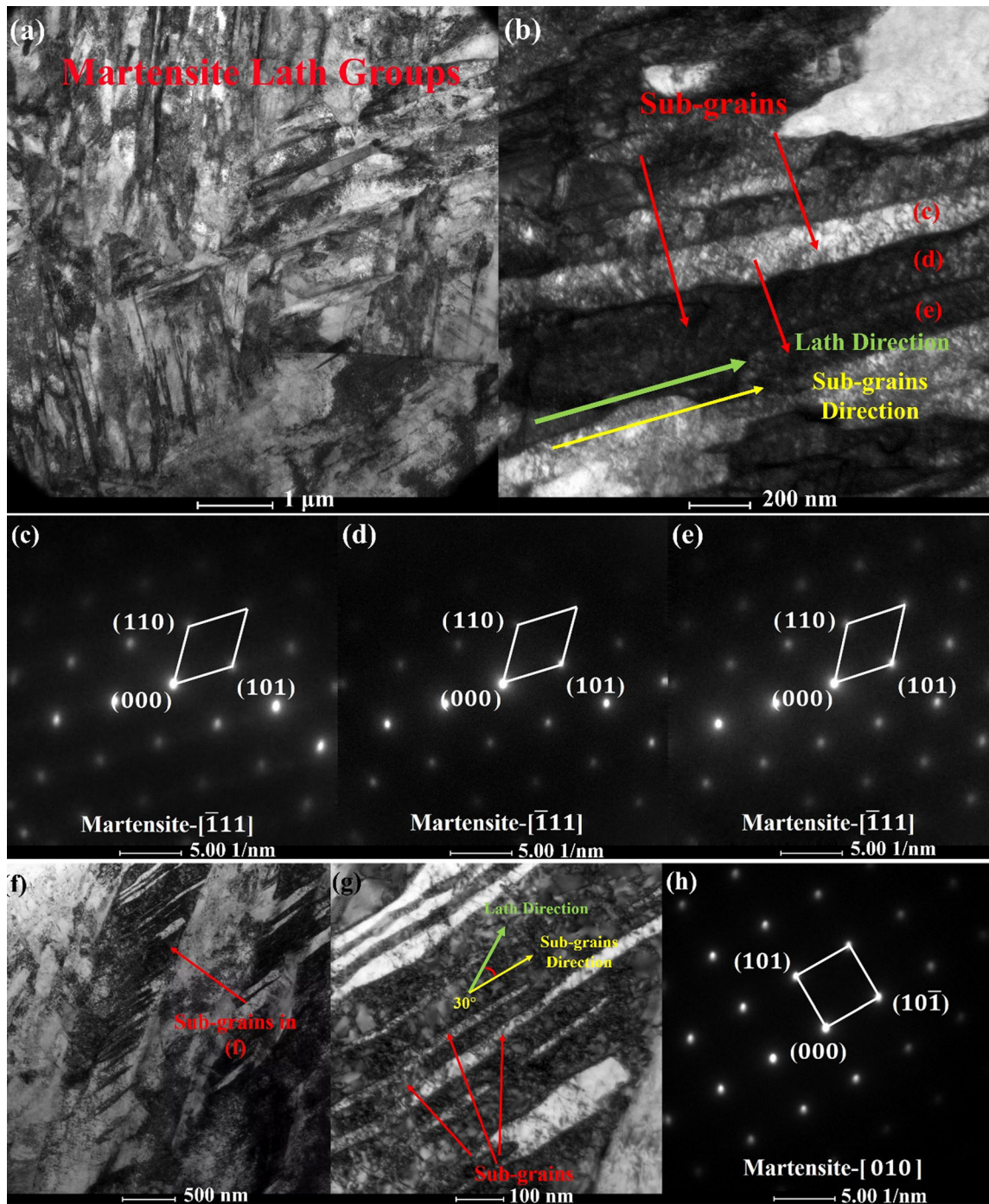


Fig. 10—TEM images showing the microstructure features in OS sample: (a) martensite lath groups, (b) laths with approximately parallel orientation in one group, (c) through (e) SAED patterns of the laths marked by (c), (d) and (e) in (b), respectively, demonstrating the sub-grain relationship, and (f) through (h) fine sub-grains in a coarse martensite lath with a certain angle to the lath direction and its SAED pattern.

substructure evolution during total 60 cycles of RHSL treatment. Such three stages have strict one-to-one correspondence to the three stages in Figure 9. From TEM observation of the samples during total 60 cycles of RHSL treatment, it is concluded that the evolution of deformation twins in the A-steel experiences three stages, early nurturing (Stage I), medium-term abundantly forming (Stage II) and later de-twinning (Stage III).

D. Mechanical Properties

Figure 20 illustrates the representative stress-strain curves of A-steel in different states. To clearly show these curves, the engineering stress–engineering strain curves and corresponding true stress–true strain curves of the samples are drawn in three figures, respectively. According to the data obtained from tensile test, the mechanical properties of A-steel in different state are

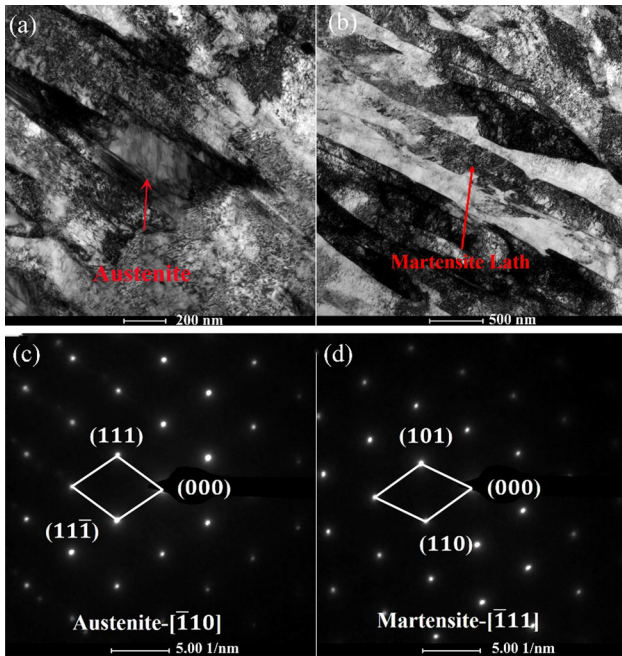


Fig. 11—TEM images and the corresponding SAED patterns showing the substructure in 927-001 sample: (a and c) austenite, and (b and d) martensite laths.

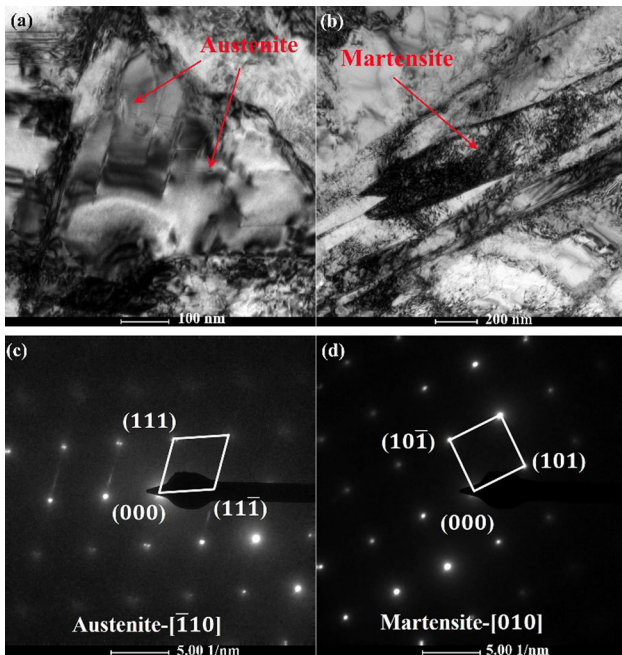


Fig. 12—TEM images and the corresponding SAED patterns showing the substructure in 927-005 sample: (a and c) austenite, and (b and d) martensite laths.

summarized in Table III, where, $\sigma_{0.2}$ is the yield strength (the yield strength of the OS sample is re-measured here, close to the known value of 927 MPa), E the elasticity modulus, σ_b the ultimate tensile strength, δ the elongation to fracture, n the strain-hardening exponent. Additionally, PSES is defined as the product of the yield strength, elongation and strain-hardening

exponent here, which characterizes the comprehensive strength-toughness of material. The reason to create this parameter is that: materials with high strength–low elongation and those with low strength–high elongation may have approximate product, which cannot be used to differentiate the comprehensive property of these materials intuitively. Strain-hardening exponent (n) reflects the strain-hardening ability involving plastic deformation ability and consequent hardening ability, which is highly related to the variation of twins (this will be discussed later). Hence, PSES is defined to reflect the influence of twins on the comprehensive property of the A-steel emphatically.

From Table IV, it is seen that the key indicators of mechanical properties of A-steel have clear variation trends with the loading cycle number, which can be divided into three stages, same as the category in microstructure evolution. In Stage I (from 0 to 10 cycles): the yield strength increases from 915 to 1152 MPa and the elastic modulus from 191 to 230 GPa; however, the elongation decreases from 16.6 to 11.7 pct and the n value from 0.129 to 0.075; the comprehensive indicator, PSES value, decreases from 1959 to 1011 MPa·pct. RHSL treatment in Stage I makes the A-steel hardened continuously. In Stage II (from 10 to 30 cycles), the steel seems to be softened, presenting as: the reductions in both the yield strength and elastic modulus from the high level in prior stage; the recoveries in both elongation and strain-hardening exponent; as a result, the PSES value recovers to 2195 MPa·pct. In Stage III (from 30 to 60 cycles), the steel again experiences a hardening process, with re-increases in both the yield strength and elastic modulus as well as the re-decreases in both elongation and strain-hardening exponent. As a results, PSES value again re-decreases to 1261 MPa·pct.

30-Cycle RHSL-treated sample has the best comprehensive mechanical properties, with high yield strength (1060 MPa), the highest elongation (19.0 pct) and highest PSES value (2195 MPa·pct), increased by about 16, 21 and 19 pct, respectively, compared to those of OS sample. It should be noted that the 927-030-sample possesses the highest fraction of twins among all the samples (Figure 9(a)). In addition, 10-cycle RHSL treatment produces the largest rises in yield strength (from 915 to 1152 MPa by about 26 pct) and elastic modulus (from 191 to 230 GPa by 20 pct), however, the elongation and strain-hardening exponent are the lowest too (11.7 pct and 0.075, respectively).

IV. DISCUSSION

A. Microstructure Evolution by RHSL Treatment

In our previous study,^[33] it was thought that, in total 20-cycle RHSL treatment to the A-steel, the first 10 cycles led to dislocation proliferation and piling-up, and twinning occurred in the second 10 cycles. However, more detailed microstructure evolution was unclear. Hence, in this study, more state points of sample produced by RHSL treatment are added.

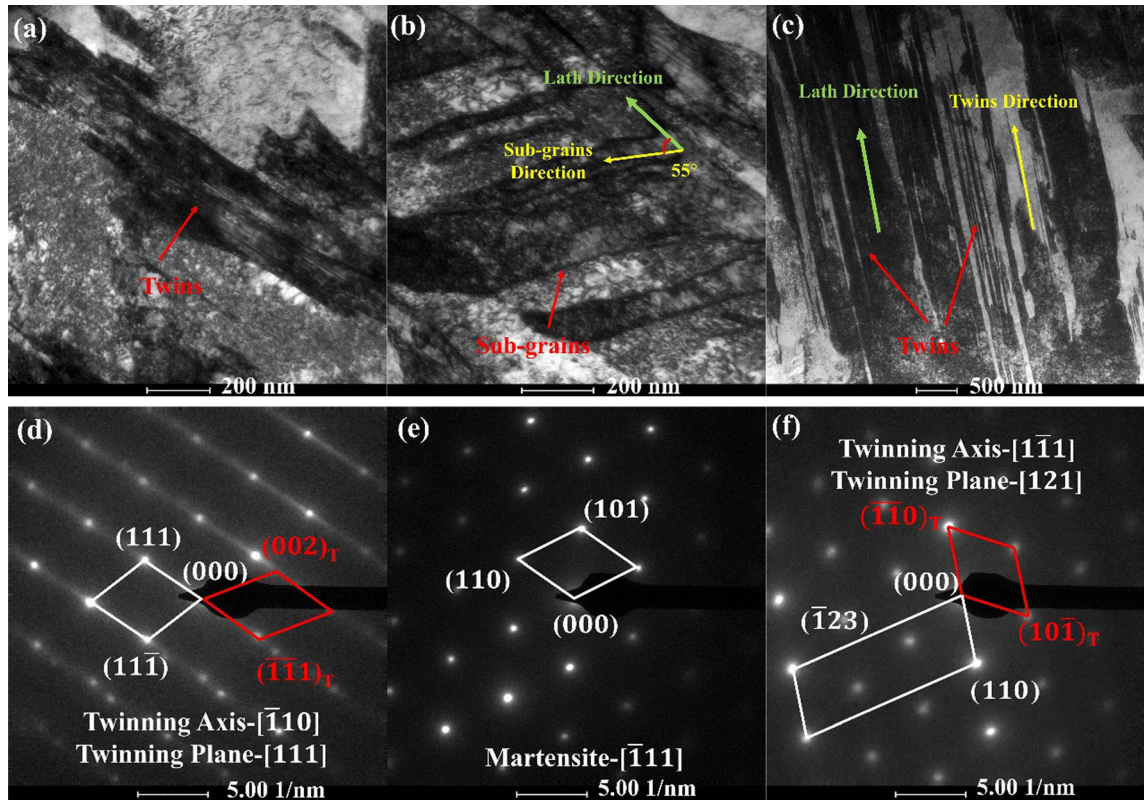


Fig. 13—TEM images and the corresponding SAED patterns showing the substructure in 927-010 sample: (a and d) twins in austenite, (b and e) sub-grains in martensite with a certain angle to the lath direction, and (c and f) Type C twins in martensite parallel to the lath direction.

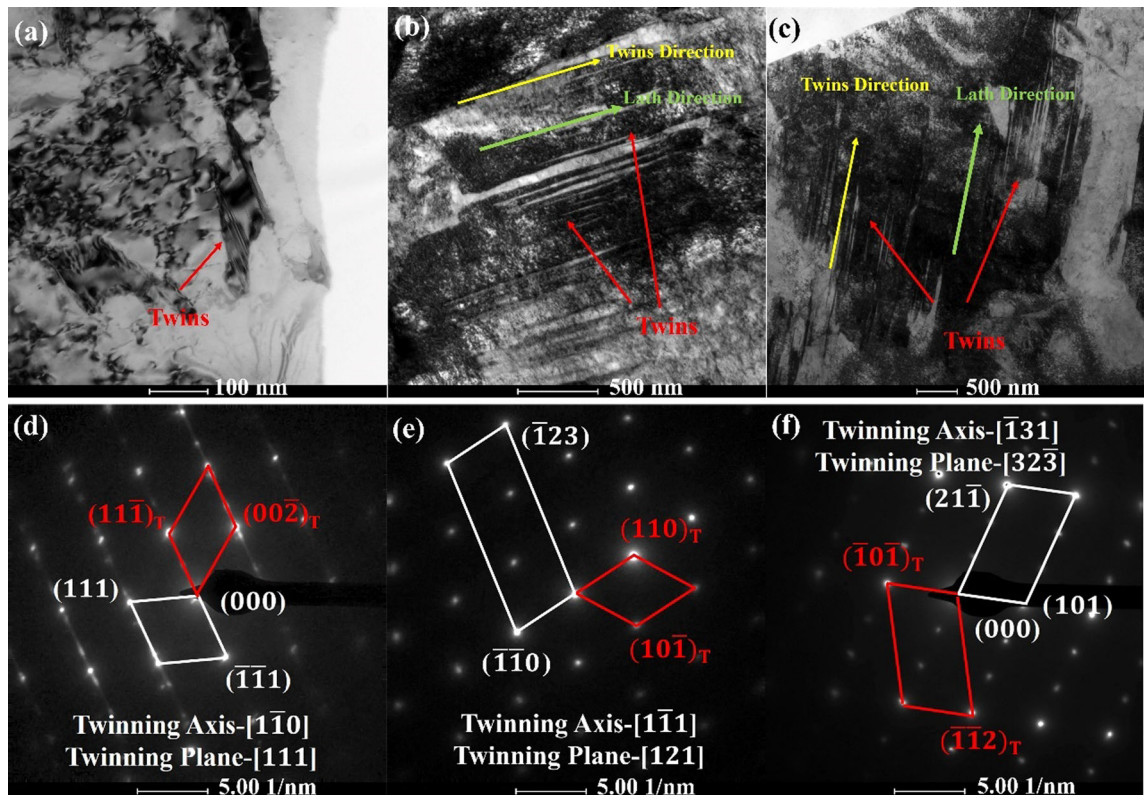


Fig. 14—TEM images and the corresponding SAED patterns showing the substructure in 927-015 sample: (a and d) twins in austenite, (b and e) Type C twins in martensite parallel to the lath direction, and (c and f) Type B twins in martensite parallel to the lath direction.

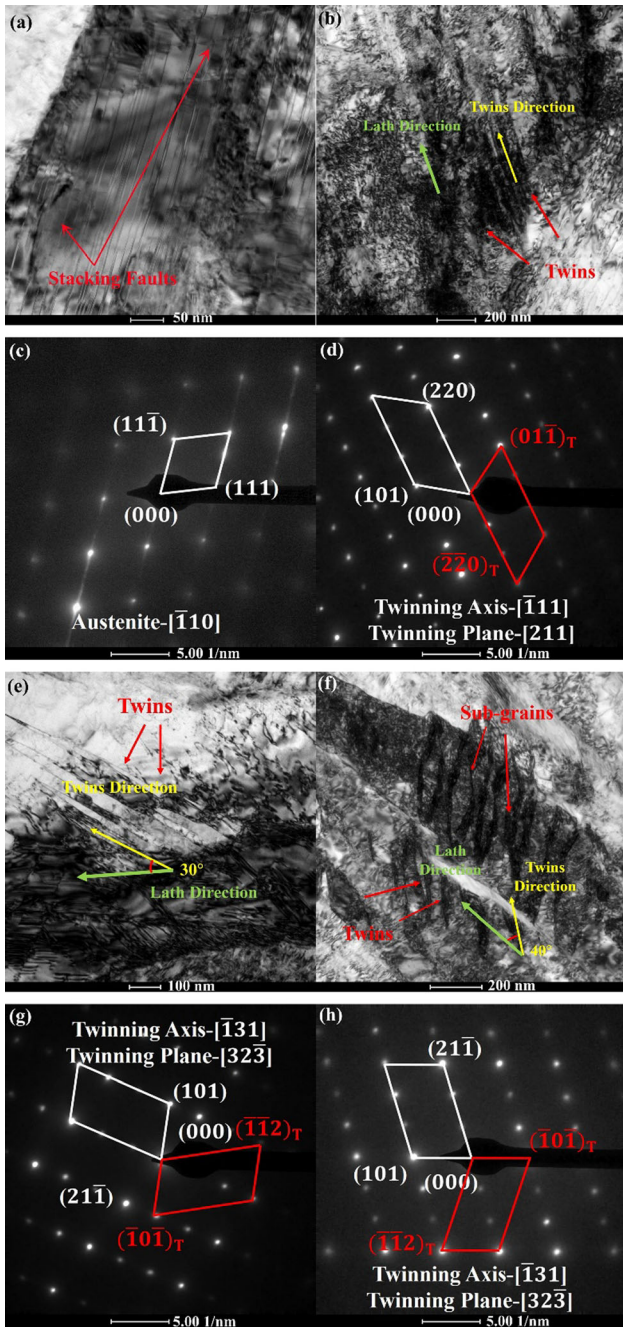


Fig. 15—TEM images and the corresponding SAED patterns showing the substructure in 927-025 sample: (a and c) SFs in austenite, (b and d) Type A twins in martensite parallel to the lath direction, (e and g) Type B twins in martensite at a certain angle to the lath direction, and (f and h) Type B twins in martensite at a certain angle to the lath direction.

Figure 21 illustrates XRD diagrams containing log data of the A-steel in different states. All samples are with three characteristic peaks of martensite, where the main peak (around $2\theta \approx 44.4$ deg) is accompanied with two small peaks (around $2\theta \approx 64.5$ and 81.8 deg). In addition, one weak peak of austenite can be seen (around $2\theta \approx 44.3$ deg) where the arrows point, indicating the existence of the small amount of austenite. From the structural information from XRD diagrams

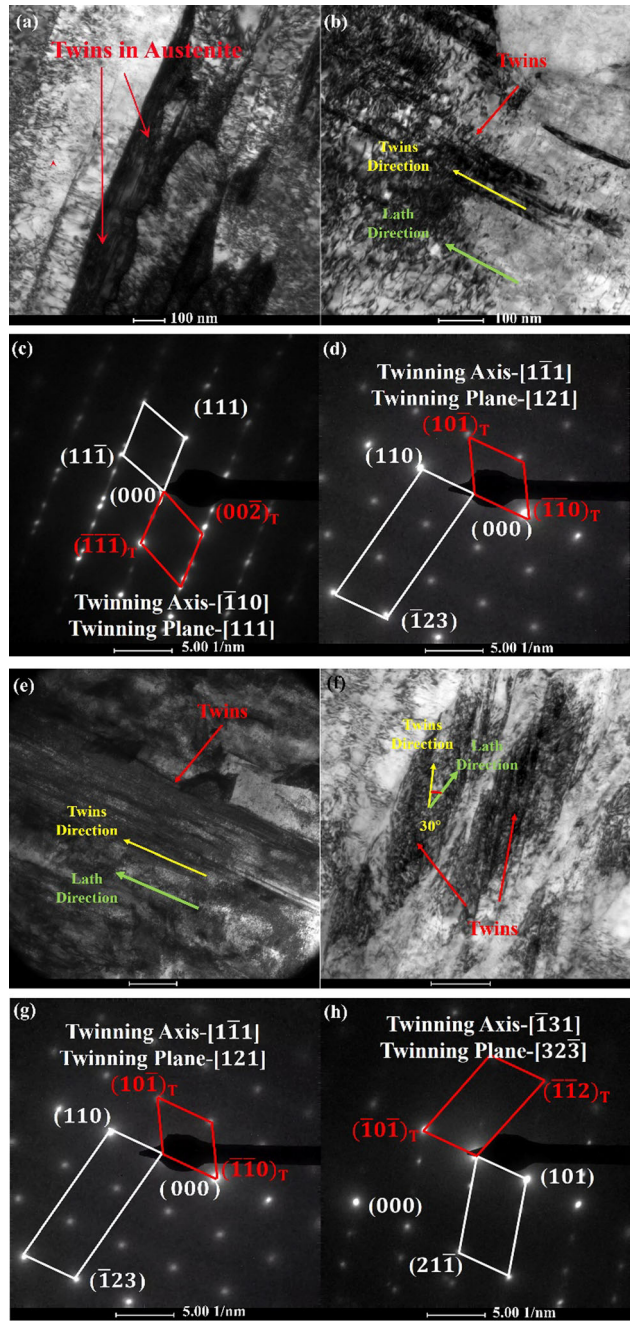


Fig. 16—TEM images and the corresponding SAED patterns showing the substructure in 927-030 sample: (a and c) twins in austenite, (b and d, e and g) Type C twins in martensite, parallel to the lath direction, and (f and h) Type B twins in martensite with a certain angle to the lath direction.

with the modified WH method, dislocation density (ρ) in the material can be calculated by Eqs. [1] through [3]. They are listed in Table IV. With the cycle number of RHSL treatment, the dislocation density is first increased to the highest value ($5.7165 \times 10^{16} \text{ cm}^{-2}$, 10-cycle), then decreased to the lowest ($5.6296 \times 10^{16} \text{ cm}^{-2}$, 30-cycle), and then increased again. 10-Cycle and 30-cycle are two special state points.

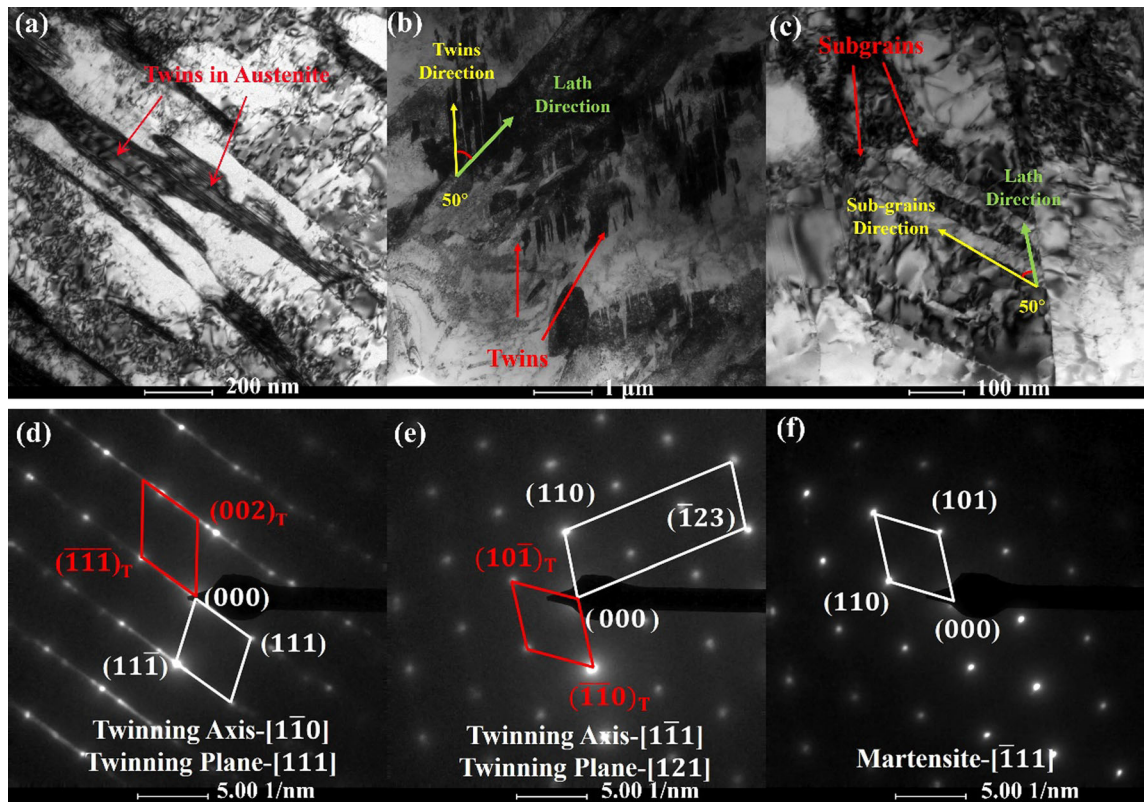


Fig. 17—TEM images and the corresponding SAED patterns showing the substructure in 927-040 sample: (a and d) twins in austenite, (b and e) Type C twins in martensite with an angle to the lath direction, and (c and f) sub-grains in martensite with a certain angle to the lath direction.

To exhibit the variation of stress concentration of the samples in different states intuitively, the representative KAM (Kernel Average Misorientation, calculated by local misorientation of each adjacent points) maps of each sample and average KAM value curve with the cycle number are shown in Figures 22 and 23, respectively. The average KAM value of one sample is the average value of the KAM values of all EBSD-scanned spots in five KAM maps. It reflects the total stress state and the stress concentration level of each sample. As shown in Figure 23, the average KAM value is increased from the original value of 0.66 to the top value of 0.78 as the loading cycle comes to 10. RHSL treatment in Stage I leads to a high level of KAM value and the peak emerges at 10-cycle state point. As described above, in 1- and 5-cycle states, there are no considerable changes of microstructure in TEM observation (Figures 11 and 12), and the variation in dislocation density is not much significant (by 0.17 and 0.26 pct compared with the OS state, respectively). However, in the 10-cycle state, the dislocation density in the sample rises obviously by 1.59 pct (compared with the OS state) and the formation of new deformation twins are obviously observed. Such increase of the dislocations must lead to severe stress concentration. Traditionally, stress concentration occurs in one-off huge plastic deformation with high stress (up to several GPa) or high strain rate (up to 10^3 s^{-1} or even higher).^[34–38] During the RHSL treatment in this study, the applied stress is only 927 MPa, thus, the high stress

concentration and strain energy are continuously accumulated in each loading cycle. Under such severe stress concentration, the main mode of further deformation begins to transfer to twinning. This is the reason for the obvious appearance of deformation twins in the 927-010-sample. However, the fraction of twins at this state still keeps at a low level as shown in Figure 9.

When the loading cycle number is further increased to 15, the dislocation density in the sample is quickly decreased to $5.6640 \times 10^{16} \text{ cm}^{-2}$ and the average KAM value accordingly drops to 0.74. At the same time, a high fraction of twins is formed and twin type becomes diversified (seen in Figures 9 and 14). These indicate that the previously accumulated stress concentration and strain energy are released by twinning and a great number of dislocations disappear. During the loading cycles from 15 to 30, by such twinning, the dislocation density further drops to $5.6296 \times 10^{16} \text{ cm}^{-2}$ (even lower than that in OS state) and the corresponding average KAM value drops to 0.71. Meanwhile, the fraction of twins is increased to the top level (Figure 9) and the diversified-types of deformation twins are generated and developed in large area in the A-steel (seen in Figures 14, 15, and 16).

When the loading cycle number further comes to 40 to 60, the dislocation density is again increased to 5.6365×10^{16} to $5.6414 \times 10^{16} \text{ cm}^{-2}$, and the corresponding average KAM value is re-increased to 0.73 to 0.75. It suggests the accumulation of stress

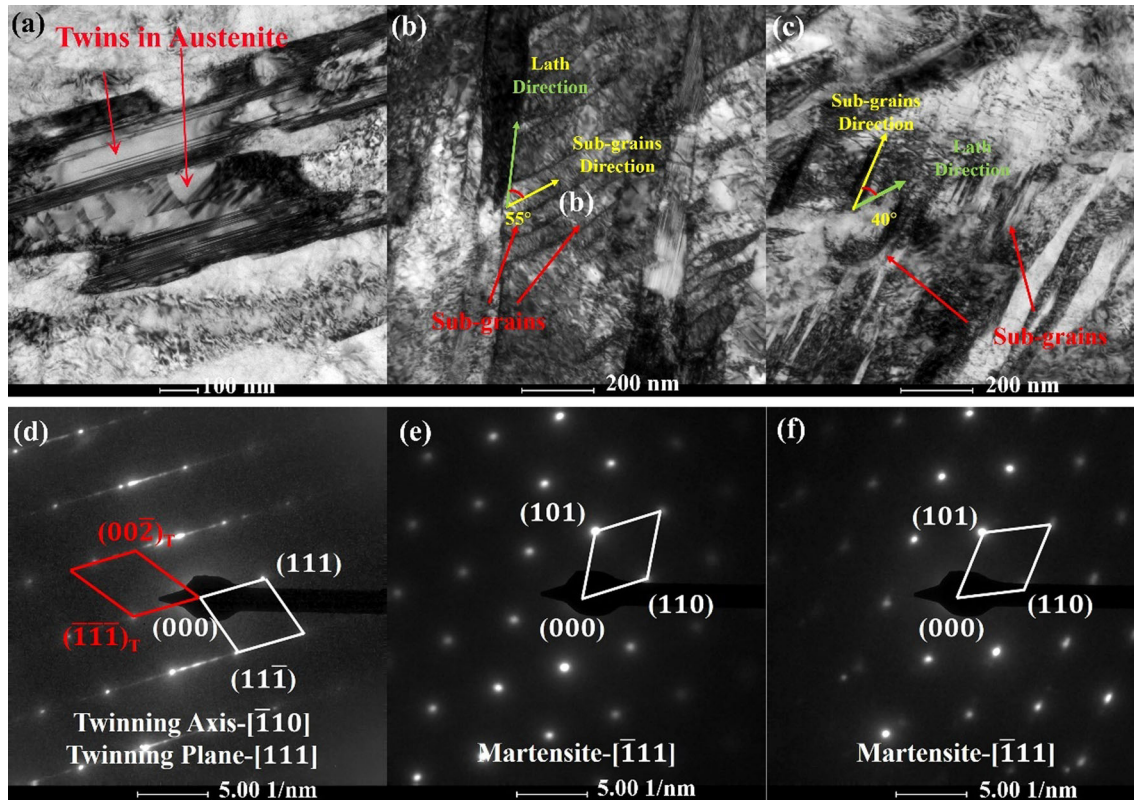


Fig. 18—TEM images and the corresponding SAED patterns showing the substructure in 927-050 sample: (a and d) twins in austenite, and (b and e, c and f) sub-grains in martensite with a certain angle to the lath direction.

concentration and strain energy is re-reinforced. On the other hand, the fraction of twins is declined (Figure 9). In austenite, de-twinning process happens in two ways, including the reduced TBs in austenite (Figure 18(a)) or being swallowed up by the new-nucleated austenite grains (Figure 19(a)). The repetitive loading/unloading treatment provides the driving force for twinning, and also for de-twinning. It is reported that the formation and migration of incoherent twin boundaries controls de-twinning process in FCC metals by mechanical treatment or heat treatment.^[54,55] In martensite laths, twins are reduced and replaced by the newly formed sub-grains (Figures 14(f), 18(c), 19(b) and (e)). Gutierrez-Urrutia *et al.*^[55] found that de-twinning in BCC-Ti alloys was caused by the boundary migration and dislocation re-arrangement driven by the annealing treatment with the temperature higher than 900 °C. Under such treatment, the deformation twins were destructed through the rotation of twin boundaries, and the accompanying recovery process led to the formation of sub-grain structure. In this study, twinning or de-twinning are due to the accumulation or release of local stress concentration induced by RHSL treatment. Additionally, sub-grains shown in Figures 13(b), 15(f), 17(c), 18(b) and 19(f) suggest that the high-density dislocations assemble and tangle to form dislocation walls that can cut the martensite laths into finer parts, namely, the sub-grain, and this process relates to the consumption of dislocations.^[56–58]

B. The Relationship Between Microstructure Evolution and Mechanical Properties

In this study, with the increase of cycling number of RHSL treatment from 1 to 60, A-steel experienced hardening–softening–re-hardening three stages. The hardening comes from the significant proliferation of dislocations, namely, strain strengthening. Surely, TBs and SGBs have contributions for the strengthening of matrix to an extent, but the contribution from strain strengthening is dominant. The softening comes from the abundant formation of deformation twins, namely, structure-softening. The relationships of the yield strength with the dislocation density and the elongation with the fraction of TBs are linked as illustrated in Figures 24(a) and (b), respectively. Here, the fraction of TBs is chosen to reflect the content of twins because twin boundaries always play an important role in toughening.^[59]

Intuitively in Figure 24, the variation of aforementioned indicators with the loading cycle number can be clearly divided into three stages: Stage I, the hardening stage, from the OS state to the 10th cycle; Stage II, the softening stage, from the 10th cycle to the 30th cycle; Stage III, the re-hardening stage, from the 30th cycle to the 60th cycle.

In Stage I, the microstructure evolution is dominated by the significant rise in dislocation density from 5.6270×10^{16} to $5.7165 \times 10^{16} \text{ cm}^{-2}$. At the same time,

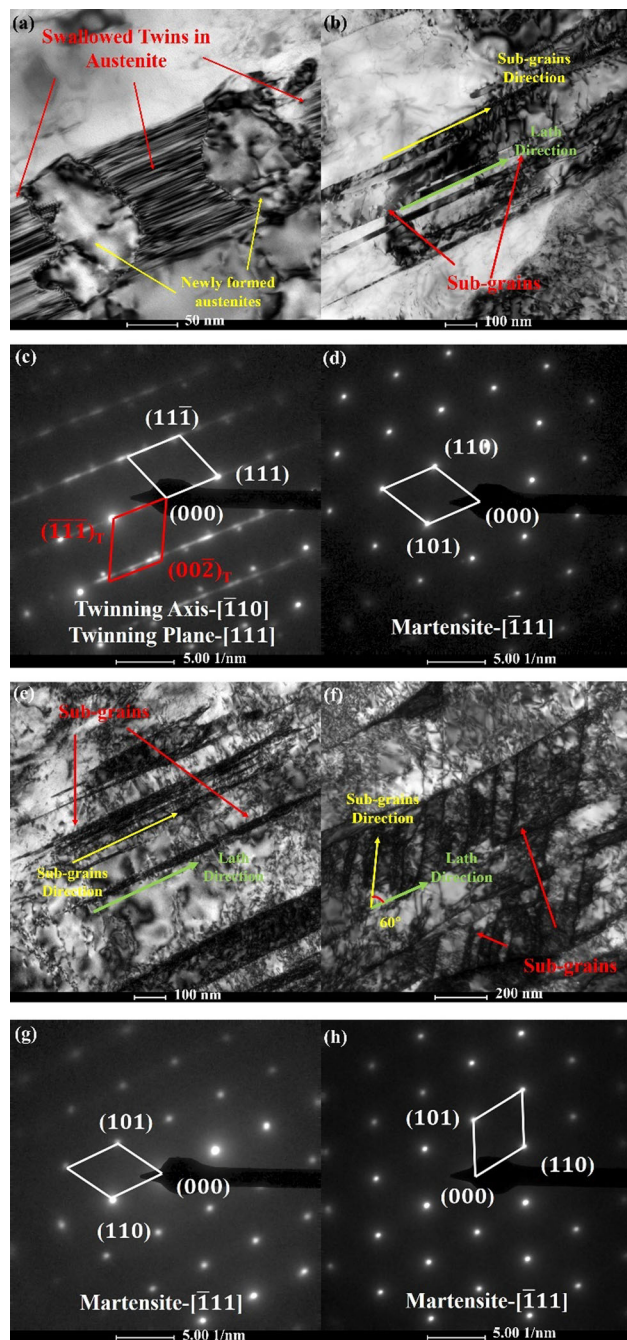


Fig. 19—TEM images and the corresponding SAED patterns showing the substructure in 927-060 sample: (a and c) detwinning in austenite, (b and d) sub-grains in martensite parallel to the lath direction, (e and g) sub-grains in martensite parallel to the lath direction, and (f and h) sub-grains in martensite at an angle to the lath direction.

the fraction of TBs is increased to 5.20 pct. Accordingly, the yield strength is increased from about 915 MPa to about 1152 MPa, while the elongation is decreased from the original 16.6 pct to about 11.7 pct and the PSES value is decreased from the original 1959 MPa·pct to about 1011 MPa·pct, indicating the improvement in

strength and the weakening in plasticity and toughness. Under the action of applied stress with the repeated loading and holding, the dislocations are increasingly proliferated. In addition, due to the severe inhomogeneity in microstructure of the A-steel, local stress concentration and strain energy are continuously accumulated that drives the formation of twins. In this stage, dislocation proliferation dominates the microstructure evolution, thus, the material is strain-hardened, *i.e.*, the increase in strength and the decrease in elongation.

In Stage II, the dominating microstructure evolution is replaced by twinning. The abundant formation of twins is accompanied with the significant decrease in dislocation density.^[59,60] With the cycle number, the fraction of TBs is rapidly increased to 13.58 pct as well as a large drop in dislocation density to $5.6296 \times 10^{16} \text{ cm}^{-2}$. The fast generation and growth of deformation twins greatly release the stress concentration and strain energy. Therefore, the material is structure-softened, presenting as recoveries in elongation to about 19.0 pct and PSES value to 2195 MPa·pct (even higher than those of the OS samples) but a reduction in yield strength to 1060 MPa. Many previous studies reported that the alloys containing abundant twins were of high ductility and deformability,^[20,61] since the twin boundaries can act as the sources for the continuous dislocation-slipping. Several interaction mechanisms between the dislocations and twin boundaries have been reported yet.^[20] Twin boundaries can help the generation of new dislocations and subsequent gliding.^[14,17] Although the dislocation density of the 30-cycle RHSL-treated sample is even lower than that of the OS, the yield strength is still higher. It is attributed to the combination of the strain-hardening effect of dislocations and the strengthening effect of twin boundaries.^[62,63]

Twinning-Induced Plasticity (TWIP) effect, which realizes the combination of high strength and high ductility, is important not only for materials with low crystal symmetry such as HCP alloys, but also for BCC and FCC alloys. The TWIP is carried out through the dynamic Hall–Petch effect, *i.e.*, the dynamic refinement of the mean free path of dislocation.^[64–67]

In the deformation process of TWIP alloys, the deformation twins cut the alloy grain into finer parts. For strengthening, the long-range motion of dislocations is hindered by the fine twin boundaries, which leads to the dislocation plugging and increases the local strength. In addition, the formation of twins in the deformed parts makes them become low strain zones, which makes the plastic deformation more durable, thus this delays the formation of necking and improves the elongation of alloys.^[68,69]

In Stage III, the dominating microstructure evolution is retaken by the dislocation proliferation (the density re-rising from 5.6365×10^{16} to $5.6414 \times 10^{16} \text{ cm}^{-2}$). Meanwhile, de-twinning to sub-grains is frequently observed in martensite laths, thus, the fraction of TBs is continuously reduced from 13.58 to 5.59 pct and the

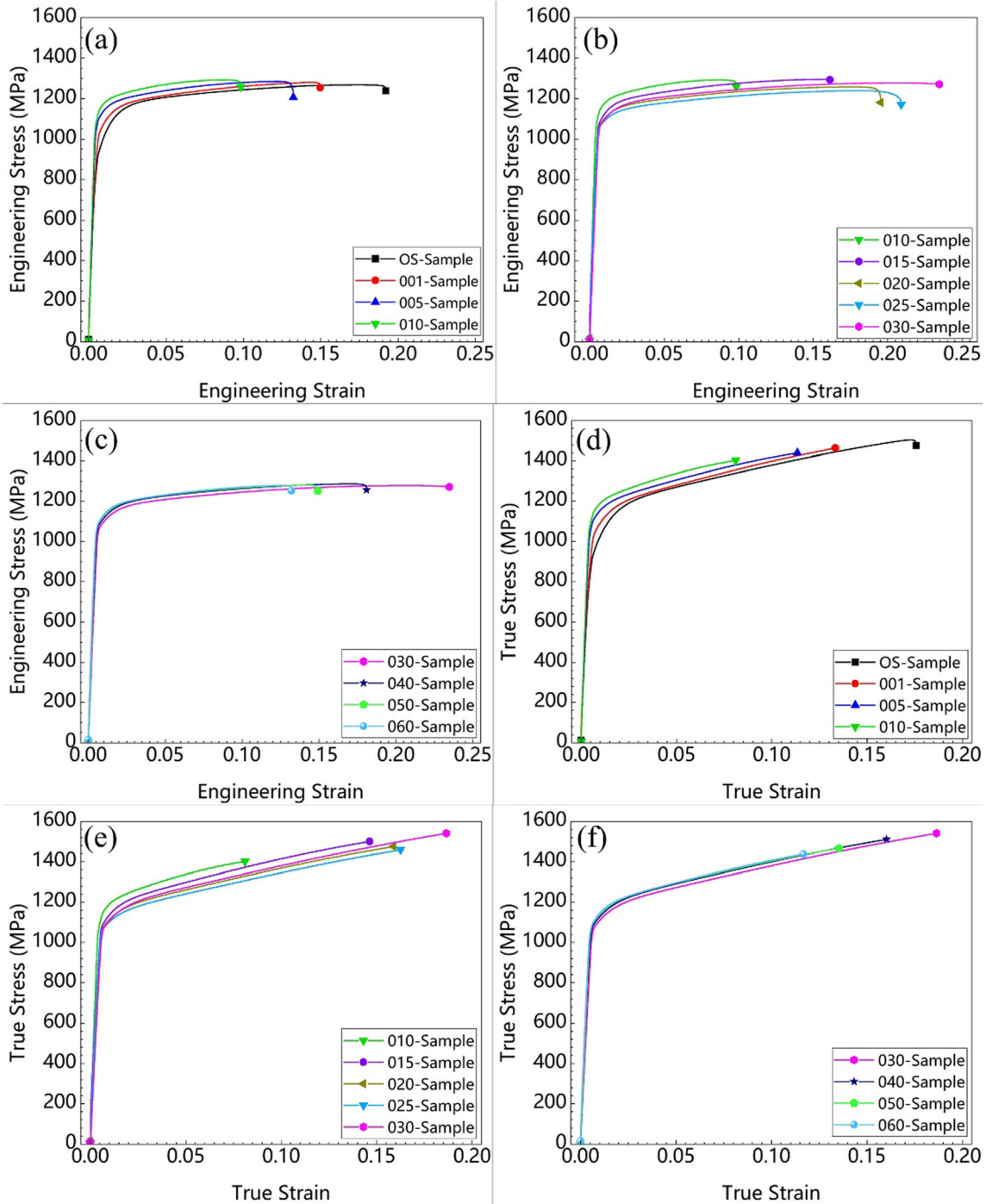


Fig. 20—Representative stress–strain curves of A-steel in different states: (a through c) engineering stress–engineering strain curves, and (d through f) corresponding true stress–true strain curves.

fraction of SGBs is increased from 70.58 to 80.08 pct. The re-proliferating of dislocations and de-twinning make the material hardened again; thus, the yield strength is recovered from 1073 to 1090 MPa while the elongation

drops from 17.4 to 13.0 pct and the PSES value drops from 1830 to 1261 MPa·pct. Besides the strain-hardening effect of dislocations, the newly formed sub-grains also have some contributions to the re-hardening. As an

Table III. Mechanical Properties of A-Steel in Different States

Sample No.	$\sigma_{0.2}$ MPa	E GPa	σ_b MPa	δ Pct	n —	PSES** MPa·Pct
OS	915 ± 3	191 ± 1	1268 ± 1	16.6 ± 0.2	0.129 ± 0.003	1959
927-001	1036 ± 12	221 ± 7	1281 ± 4	15.1 ± 0.2	0.101 ± 0.009	1580
927-005	1099 ± 13	225 ± 2	1271 ± 21	13.5 ± 0.2	0.084 ± 0.006	1246
927-010	1152 ± 10	230 ± 4	1275 ± 17	11.7 ± 0.3	0.075 ± 0.009	1011
927-015	1078 ± 13	208 ± 5	1294 ± 20	15.9 ± 0.2	0.095 ± 0.006	1628
927-020	1076 ± 10	200 ± 1	1285 ± 26	17.6 ± 0.2	0.097 ± 0.005	1837
927-025	1042 ± 7	201 ± 5	1230 ± 11	18.2 ± 0.3	0.099 ± 0.016	1877
927-030	1060 ± 3	192 ± 3	1276 ± 7	19.0 ± 0.2	0.109 ± 0.012	2195
927-040	1073 ± 4	208 ± 6	1294 ± 9	17.4 ± 0.2	0.098 ± 0.006	1830
927-050	1084 ± 2	216 ± 2	1262 ± 19	14.7 ± 0.2	0.087 ± 0.009	1386
927-060	1090 ± 5	224 ± 6	1277 ± 9	13.0 ± 0.3	0.089 ± 0.002	1261

**PSES: the product of the yield strength, elongation and strain-hardening exponent.

Table IV. Dislocation Density in the A-Steel in Different States by Modified Williamson–Hall Method

Sample No.	ρ 10^{16} cm^{-2}	Sample No.	ρ 10^{16} cm^{-2}	Sample No.	ρ 10^{16} cm^{-2}
OS	5.6270	927-015	5.6440	927-040	5.6365
927-001	5.6366	927-020	5.6438	927-050	5.6390
927-005	5.6414	927-025	5.6318	927-060	5.6414
927-010	5.7165	927-030	5.6296	—	—

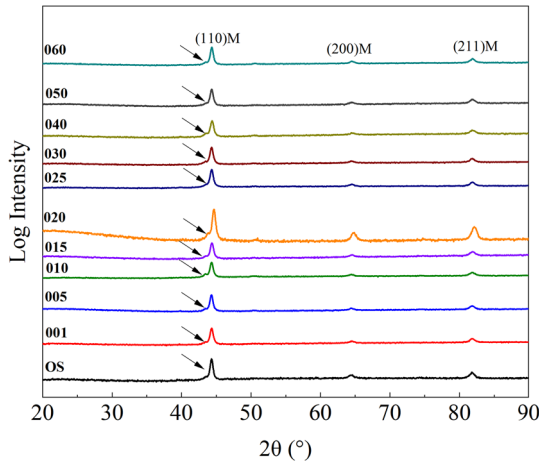


Fig. 21—XRD diagrams of A-steel in different states.

interface, the growing sub-grain boundaries is able to become the barriers for dislocation-slipping.^[70]

As shown in Figure 24, YS is non-monotonically varying with the dislocation density. But, from

Figure 24, it is rational to conclude that the variation of yield strength is strongly correlated with the increase or decrease of dislocation density induced by the RHSL treatment, and elongation is highly related to the fraction of twins existing.

V. CONCLUSIONS

Repetitive high stress loading/unloading treatment under the holding stress of 927 MPa with different loading cycle number was applied on A-steel to verify its influences on the substructure evolution and mechanical properties. The main conclusions were obtained as follows.

- (1) From the results of strain–time curves of all samples, it is seen that total 60 cycles RHSL treatment with a low strain rate (less than $128 \times 10^{-3} \text{ s}^{-1}$) only produces tiny plastic deformation (residual strain less than 0.011).
- (2) The microstructure evolution of the A-steel during total 60 cycles of the RHSL treatment can be divided into three stages. In Stage I (the first 10

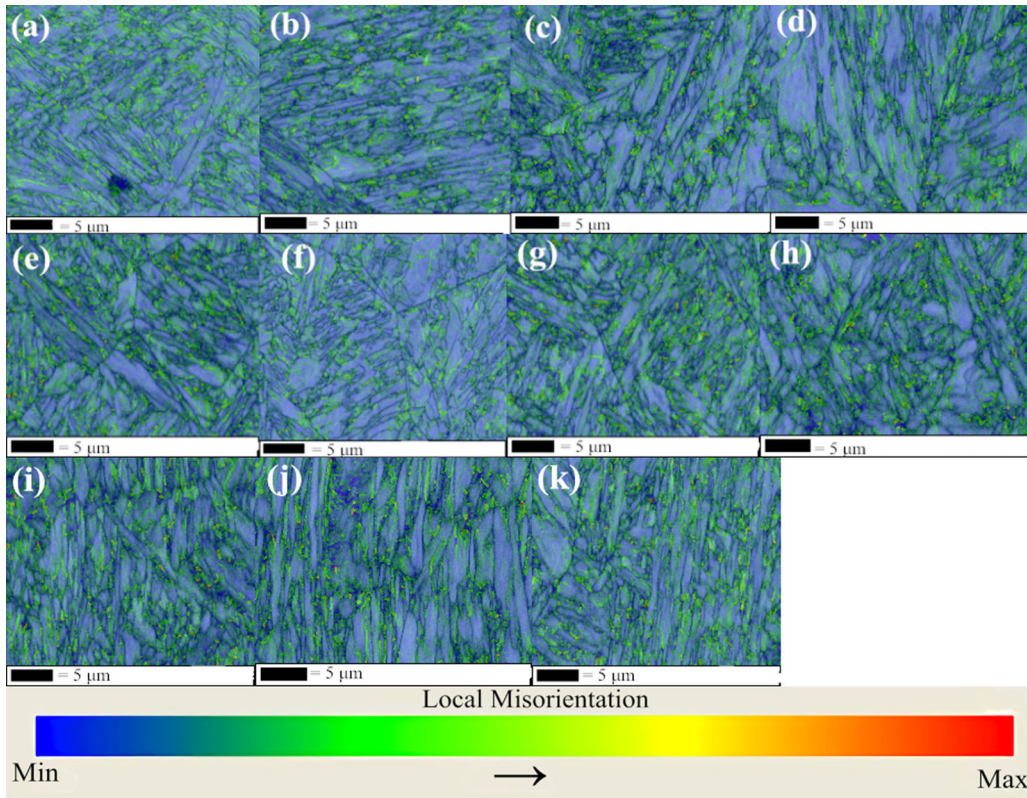


Fig. 22—KAM maps of the samples with/without the RHSL treatment: (a) OS, (b) 927-001, (c) 927-005, (d) 927-010, (e) 927-015, (f) 927-020, (g) 927-025, (h) 927-030, (i) 927-040, (j) 927-050, and (k) 927-060.

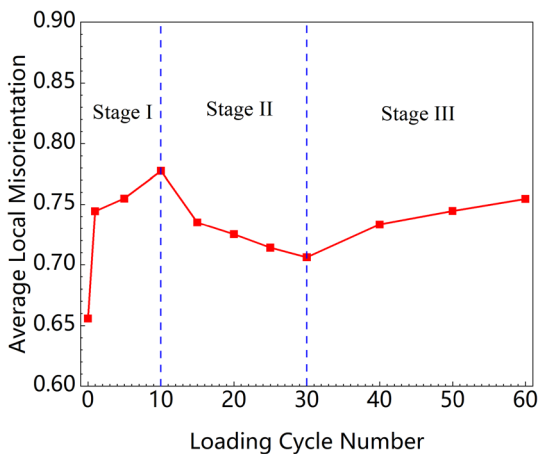


Fig. 23—Average KAM value of the samples with the cycle number of RHSL treatment.

cycles), the dislocations are rapidly proliferated, accompanied by the nurturing of deformation twins. In Stage II (the middle 20 cycles), diversified deformation twins are abundantly formed, along with the significantly decrease in dislocation density. In Stage III (the last 30 cycles), the formed twins are de-twinning into sub-grains, together with the re-increase in dislocation density. Thus, the evolution of deformation twins

- (3) The variation of mechanical properties of the A-steel during total 60 cycles of RHSL treatment can also be divided into corresponding three stages. In the Stage I (the hardening stage), due to the significant increase of dislocation density, the yield strength increases and the elongation decreases. In the Stage II (the softening stage), due to the abundant formation of twins, the yield strength decreases and the elongation recovers. In the Stage III (the re-hardening stage), due to the decrease of twins-fraction and the re-increase in dislocation density, the yield strength re-increases and the elongation re-decreases.
- (4) Yield strength is non-monotonically varying with the dislocation density but its variation is strongly correlated with the increase or decrease of dislocation density induced by the RHSL treatment, and elongation is highly related to the fraction of twins existing.
- (5) The A-steel treated by 30-cycle RHSL at room temperature (with the holding stress close to the yield strength and the loading time of 0.64 seconds) has the highest fraction of twins (13.58 pct TBs) and possesses a high yield strength (1060 MPa), the highest elongation (19.0 pct) and the highest PSES value (2195 MPa·pct).

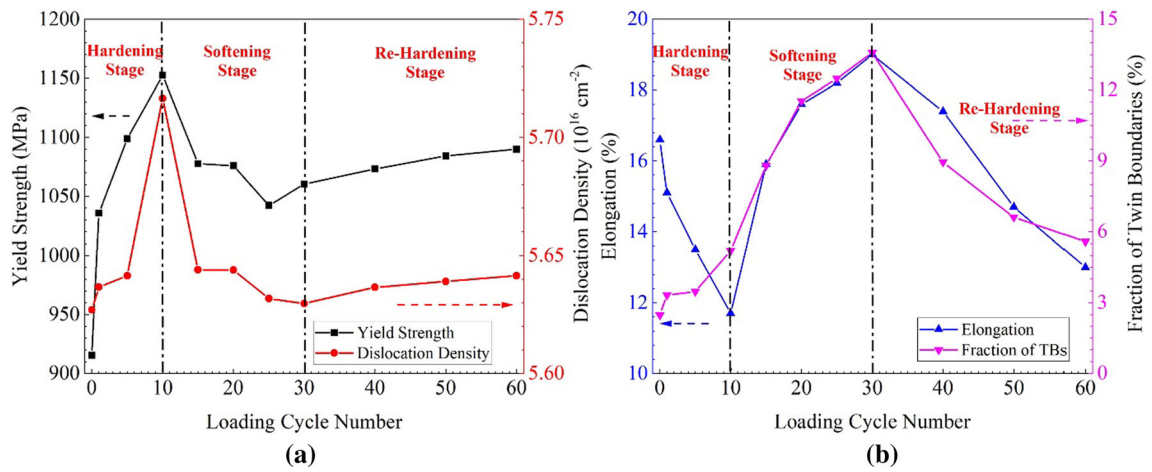


Fig. 24—Relationships of the yield strength with the dislocation density (a) and the elongation with the fraction of TBs (b).

ACKNOWLEDGMENTS

This work was funded by National Natural Science Foundation of China (Grant No. 52005385). The authors thank Dr. Aiqun Xu for TEM observation.

DATA AVAILABILITY

No additional data are available.

CONFLICT OF INTEREST

The authors declare that: no conflict of interest exists in the submission of this manuscript, and manuscript is approved by all authors for publication. The work described was original research that has not been published previously, and not under consideration for publication elsewhere, in whole or in part. All the authors listed have approved the manuscript that is enclosed.

REFERENCES

1. L. Angkurarach and P. Juijerm: *Songklanakarin J. Sci. Technol.*, 2021, vol. 43(1), pp. 1–7.
2. P. Chakraborti and M. Mitra: *Int. J. Fatigue*, 2006, vol. 28(3), pp. 194–202.
3. G. Gao, B. Zhang, C. Cheng, et al.: *Int. J. Fatigue*, 2006, vol. 28(3), pp. 194–202.
4. C. Petersen and D. Rodrian: *Int. J. Fatigue*, 2008, vol. 30(2), pp. 339–44.
5. H. Liao, H. Xu, J. Tang, et al.: *Metall. Mater. Trans. A*, 2020, vol. 51A(1), pp. 76–81.
6. S. Morito, J. Nishikawa, and T. Maki: *ISIJ Int.*, 2003, vol. 43(9), pp. 1475–77.
7. Y. Tan: *Acta Metall. Sin.*, 1985, vol. 21(3), pp. A181–86.
8. B. Sandvik and C. Wayman: *Metall. Trans. A*, 1983, vol. 14(4), pp. 823–34.
9. Z. Zhang, Y. Liu, K. Zhang, et al.: *Trans. Mater. Heat Treat.*, 2010, vol. 31(9), pp. 33–36.

10. C. Hong, N. Tao, K. Lu, et al.: *Scripta Mater.*, 2009, vol. 61(3), pp. 289–92.
11. A. Ojha, H. Sehitoglu, L. Patriarca, et al.: *Model. Simul. Mater. Sci.*, 2014, vol. 22(7), p. 075010.
12. K. Jiang, B. Gan, J. Li, et al.: *Mater. Sci. Eng. A*, 2021, vol. 816, p. 141298.
13. Y. Li, Z. Liao, W. Zhang, et al.: *Materials*, 2020, vol. 13(4732), pp. 1–8.
14. F. Zhao, T. Suo, B. Chen, et al.: *J. Alloys Compd.*, 2019, vol. 798, pp. 350–59.
15. A. Singh, L. Tang, M. Dao, et al.: *Acta Mater.*, 2011, vol. 59, pp. 2437–46.
16. F. Yan, G. Liu, N. Tao, et al.: *Acta Mater.*, 2012, vol. 60, pp. 1059–71.
17. N. Zhou, Z. Zhang, L. Jin, et al.: *Mater. Des.*, 2014, vol. 56, pp. 966–74.
18. S. Ma, L. Fu, and A. Shan: *Mater. Charact.*, 2021, vol. 177, p. 111057.
19. X. Liu, L. Sun, L. Zhu, et al.: *Acta Mater.*, 2018, vol. 149, pp. 397–406.
20. G. Zhao, X. Xu, D. Dye, et al.: *Acta Mater.*, 2020, vol. 183, pp. 155–64.
21. H. Matsumoto, H. Yoneda, K. Sato, et al.: *Mater. Sci. Eng. A*, 2011, vol. 528, pp. 1512–20.
22. X. Zhou, Y. Li, Z. Han, et al.: *Mater. Sci. Eng. A*, 2024, vol. 892, p. 146086.
23. H. Cheng, X. Li, L. Sun, et al.: *Mater. Sci. Eng. A*, 2024, vol. 900, p. 146402.
24. Y. Zhou, J. Long, J. Fan, et al.: *Mater. Charact.*, 2024, vol. 208, p. 113612.
25. S. Chiou, W. Cheng, and W. Lee: *Mater. Sci. Eng. A*, 2004, vol. 386(1–2), pp. 460–67.
26. Y. Li, N. Tao, and K. Lu: *Acta Mater.*, 2008, vol. 56(2), pp. 230–41.
27. J. Harding: *Proc. R. Soc. A*, 1967, vol. 299(1459), pp. 464–90.
28. R. Smith, J. Eggert, R. Rudd, et al.: *J. Appl. Phys.*, 2011, vol. 110(12), p. 123515.
29. T. Resseguier and M. Hallouin: *J. Appl. Phys.*, 1998, vol. 84(4), pp. 1932–38.
30. T. Resseguier and M. Hallouin: *J. Appl. Phys.*, 2001, vol. 90(9), pp. 4377–84.
31. S. Yin, H. Yang, S. Li, et al.: *Scripta Mater.*, 2008, vol. 58(9), pp. 751–54.
32. Y. Wei, H. Liao, H. Xu, et al.: *Int. J. Fatigue*, 2022, vol. 158, p. 106750.
33. Y. Wei, H. Liao, and S. Huo: *Int. J. Fatigue*, 2023, vol. 166, p. 107293.
34. L. Lu, R. Schwaiger, Z. Shan, et al.: *Acta Mater.*, 2005, vol. 53, pp. 2169–79.
35. W. Visser and H. Ghonem: *Mater. Sci. Eng. A*, 2017, vol. 687(Complete), pp. 28–38.

36. R. Rohde: *Acta Metall.*, 1969, vol. 17(3), pp. 353–63.
37. H. Rack: *Metall. Trans. A*, 1976, vol. 7(10), pp. 1571–76.
38. N. Amadou, E. Brambrink, et al.: *Metals*, 2016, vol. 6(12), p. 320.
39. The State Standard of the People's Republic of China: *GB/T 228.1-2010, Metallic Materials-Tensile Testing-Part 1: Method of Test at Room Temperature*, The State Standard of the People's Republic of China, 2010.
40. J. Chakraborty, M. Ghosh, and R. Ranjan: *Philos. Mag.*, 2013, vol. 93(46), pp. 4598–4616.
41. T. Ungar and A. Borbély: *Appl. Phys. Lett.*, 1996, vol. 69(21), pp. 3173–75.
42. M. Wilkes: *Phys. Status Solidi (a)*, 1970, vol. 2, pp. 359–70.
43. A. Borbély, J. Dragomir-Cernatescu, G. Ribárik, et al.: *J. Appl. Crystallogr.*, 2003, vol. 36, pp. 160–62.
44. Y. Song, Z. Guan, P. Ma, et al.: *Acta Metall. Sin.*, 2006, vol. 7, pp. 673–80.
45. The State Standard of the People's Republic of China: *GB/T 5028-2008, Metallic Materials-Sheet and Strip-Determination of Tensile Strain Hardening Exponent*, The State Standard of the People's Republic of China, 2008.
46. N. Malyar, B. Grabowski, G. Dehm, et al.: *Acta Mater.*, 2018, vol. 161, pp. 412–19.
47. T. Mana, T. Liu, D. Ping, et al.: *Mater. Charact.*, 2018, vol. 135, pp. 175–82.
48. R. Sedlacek, W. Blum, J. Kratochvil, et al.: *Metall. Mater. Trans. A*, 2002, vol. 33A, pp. 319–27.
49. L. Balogh, G. Ribárik, and T. Ungár: *J. Appl. Phys.*, 2006, vol. 100, p. 023512.
50. B. Xiao, Y. Chen, and M. Sui: *J. Chin. Electron Microsc. Soc.*, 2015, vol. 34(5), pp. 401–08.
51. X. An, W. Jiang, S. Ni, et al.: *Mater. Charact.*, 2023, vol. 197, p. 112674.
52. Y. Qin, G. Gotz, and W. Blum: *Mater. Sci. Eng. A*, 2003, vol. 341, pp. 211–15.
53. G. Shu, J. Liu, and C. Shi: *Microstructure, Properties and Engineering Application of T/P91 Steel for Supercritical Boiler*, Shaanxi Science and Technology Press, Xi'an, 2006.
54. J. Wang, N. Li, O. Anderoglu, et al.: *Acta Mater.*, 2010, vol. 58, pp. 2262–70.
55. I. Gutierrez-Urrutia, C. Li, and K. Tsuchiya: *J. Mater. Sci.*, 2017, vol. 52, pp. 7858–67.
56. M. Ortiz, E. Repetto, and L. Stainier: *J. Mech. Phys. Solids*, 2000, vol. 48, pp. 2077–2114.
57. H. Mughrabi: *Acta Metall.*, 1983, vol. 31(9), pp. 1367–79.
58. Q. Sun, Y. Ni, and S. Wang: *Acta Mater.*, 2021, vol. 203, p. 116474.
59. Z. Wu, Y. Zhang, and D. Srolovitz: *Acta Mater.*, 2009, vol. 57, pp. 4508–18.
60. Y. Zhu, X. Liao, X. Wu, and J. Narayan: *J. Mater. Sci.*, 2013, vol. 48, pp. 4467–75.
61. J. Hwang: *Materials*, 2020, vol. 13(10), p. 2250.
62. C. Huang, K. Wang, S. Wu, et al.: *Acta Mater.*, 2006, vol. 54, pp. 655–65.
63. P. Zhang, Y. Chen, W. Xiao, et al.: *Prog. Nat. Sci. Mater.*, 2016, vol. 26, p. 169172.
64. C. Park, J. Kim, C. Park, et al.: *Acta Mater.*, 2023, vol. 248, p. 118763.
65. B. Ellyson, K. Fezza, T. Sun, et al.: *Mater. Sci. Eng. A*, 2022, vol. 857, p. 143716.
66. C. Hung, Y. Bai, T. Shimokawa, et al.: *Sci. Rep. UK*, 2011, vol. 11, p. 8468.
67. R. Liu, Z. Liang, L. Lin, et al.: *Acta Metall. Sin.*, 2021, vol. 34, pp. 169–73.
68. H. Ding, Z. Tang, W. Li, et al.: *J. Iron. Steel Res. Int.*, 2006, vol. 13(6), pp. 66–70.
69. I. Gutierrez-Urrutia and D. Raabe: *Acta Mater.*, 2011, vol. 59(16), pp. 6449–62.
70. P. Zhang, H. Wang, C. Wang, et al.: *Mater. Sci. Eng. A*, 2019, vol. 766, p. 138331.

Publisher's Note Springer Nature remains neutral with regard to jurisdictional claims in published maps and institutional affiliations.

Springer Nature or its licensor (e.g. a society or other partner) holds exclusive rights to this article under a publishing agreement with the author(s) or other rightsholder(s); author self-archiving of the accepted manuscript version of this article is solely governed by the terms of such publishing agreement and applicable law.